

**Deanship of Graduate Studies
Al – Quds University**



**Structural Stability of Magnetocaloric Mn_4FeSi_3 under High-
Pressure**

Mohammad Akram Nemer Maswada

M.Sc. Thesis

Jerusalem – Palestine

1437/2016

Structural Stability of Magnetocaloric Mn_4FeSi_3 under High-Pressure

Prepared By

Mohammad Akram Nemer Maswada

B. Sc., Applied Physics, Palestine Polytechnic University Palestine

Supervisors

Prof. Salman M. Salman

Physics Department, Al-Quds University, Palestine

PD Dr. Karen Friese

Jülich Centre for Neutron Science-2, FZJülich, Germany

**A thesis submitted in partial fulfillment of the requirements
for the degree of Master of Science in Physics**

Jerusalem – Palestine

1437/2016

Al – Quds University
Deanship of Graduate Studies
Physics Department



Thesis Approval

Structural Stability of Magnetocaloric Mn_4FeSi_3 under High Pressure

Prepared by: Mohammad A. Maswada

Registration No: 21120182.

Supervisors

Prof. Salman M Salman, Physics Al-Quds University, Palestine.

Dr. Karen Friese, Jülich Centre for Neutron Science-2, FZJülich, Germany

Master thesis submitted and accepted, 3 /1 /2016, Names and signatures of examining committee members:

1. Head of the committee: Prof. Salman M Salman
2. Internal Examiner: Prof. Musa Abut air
3. External Examiner: Prof. Jamal Gabon

Signature: *S.M. Salman*
Signature: *Musa Abut air*
Signature: *Jamal Gabon*

Jerusalem-Palestine

1437/ 2016

Dedication

I lovingly dedicate this thesis to my family for their endless love, support and encouragement. Especially, to my father, to my mother for her patience and understanding, to my wife Huda Maswada and to my daughter Rital Maswada for opening my eyes to the world.

Declaration

I, Mohammad A. Maswada, declare that this thesis “**Structural Stability of Magnetocaloric Mn_4FeSi_3 under High Pressure**” and the work presented in it are my own and that it has been generated by me as the result of my own original research and that it has not been submitted earlier elsewhere.

I confirm that this work was done under the supervision of Professor Salman M. Salman from the Physics Department, Al-quds University, Palestine, and PD Dr. Karen Friese from the Jülich Centre for Neutron Science-2, Research Center Jülich GmbH, Germany.

Mohammad A. Maswada

Jerusalem – Palestine

1437/2015

This project is part of a collaborative effort under the under the SCP-2 of the framework collaboration between Research Center Jülich GmbH, Germany, and the Alquds University, Palestine, and coordinated by Professors Claus Schneider the head of Peter Grünberg Institute, Electronic Properties (PGI-6) and Salman M Salman from Physics and Director of Alquds Jülich Cooperation Program at Alquds University.



Acknowledgements

First, I thank Allah due to his blessings, I could finish my thesis. I would like to thank my beloved parents and family for their encouragement who were so supportive to me throughout my life.

It is important to thank those people who have contributed to the development of this thesis. Thanks, first of all, to Prof. Salman M. Salman for giving me a chance to conduct the practical part of this thesis within the framework collaboration between Al-Quds University and Research Center Jülich*. Thanks and appreciation to Dr. Karen Friese for supporting my work in every sense and providing excellent working conditions in her institute. In addition, I would like to thank Prof. Brückel for accepting me as a Master student in his institute, and Andrzej Grzechnik for support with the diamond anvil cell experiments. I also thank Michael Hanfland for help during the experiments at the ESRF.

Last but not least, I also thank my friends and my teachers, for providing support. I would like to specially thank Sadam Hazaimh and Abdulrahman, and Paul Hering for being supportive throughout my time in Germany.

Mohammad A. Maswada

Abstract

The magneto caloric compound Mn_4FeSi_3 crystallizes hexagonal (space group $P6_3/mcm$) at ambient conditions. The focus of this work was on the crystal structure analysis of the compound Mn_4FeSi_3 under high pressure using in situ X-ray powder and single crystal diffraction at laboratory and synchrotron sources in diamond anvil cells. Measurements were carried out in the pressure range from 0.0001 GPa to 11.0 GPa. The response of the lattice parameters and the interatomic distances to the applied hydrostatic pressure has been characterized in detail.

Contents	Page
Abstract	lii
List of Tables	Vi
List of Figures	Vii
List of Abbreviations	X
<i>Chapter 1: Introduction</i>	1
1.1 About this work	1
1.2 Overview of this research	2
<i>Chapter 2: Background</i>	3
2.1 The magnetocaloric effect.....	3
2.2 Previous work on compounds of the series $Mn_{5-x}Fe_xSi_3$ (x=0-5)	3
<i>Chapter 3: Theoretical Concepts</i>	5
3.1 Some basic concepts of Crystallography.....	5
3.2 X-Ray Diffraction and Bragg's Law.....	6
3.3 Ewald sphere construction	7
3.4 X-Ray Powder Diffraction	8
3.5 The structure factor	8
3.5.1. The Phase Problem of X-ray Crystallography.....	9
<i>Chapter 4: Experimental Techniques</i>	10
4.1 Synthesis of the single crystal of $Mn_{5-x}Fe_xSi_3$ with x=1	10
4.2 Single Crystal X-ray Crystallography	11
4.2.1 Single crystal diffraction at ambient pressure	12
4.3 Single crystal diffraction under high pressure	13
4.3.1 The diamond anvil cell (DAC)	14
4.3.2 Pressure measurements with ruby fluorescence	16

<i>Chapter 5: Experimental Procedures</i>	18
5.1 Crystal Structure Determination at ambient pressure	18
5.1.1 Crystal selection	19
5.1.2 Mounting the sample	20
5.1.3 Search for reflections	21
5.1.4 Data Reduction and Corrections	23
5.1.5 Structure Determination	24
5.2 Single Crystal Structure Determination at High Pressure	29
5.2.1 Loading the sample into the diamond anvil cell	29
5.2.2 Data collection	29
5.2.3 Data Reduction and Corrections	31
5.2.4 Data refinement and structure solution	33
<i>Chapter 6: Powder Diffraction</i>	37
6.1 High Pressure X-Ray Powder Diffraction	37
6.2 Processing of the powder diffraction data.....	38
6.3 Equation of State “EOS”	39
<i>Chapter 7: Results and discussion</i>	40
7.1 Crystal structure of Mn_4FeSi_3 at ambient conditions.....	40
7.2 Effect of pressure on the lattice parameter and unit cell volume...	41
7.3. Pressure dependence of the interatomic distances in Mn_4FeSi_3 ...	45
7.4. Effect of pressure on the crystal structure of Mn_4FeSi_3	49
<i>Chapter 8: Summary and Conclusions</i>	50
<i>Bibliography</i>	51

List of Tables

Chapter 5

Table 5.1: Data collection parameters for measurements on Mn_4FeSi_3 at ambient conditions.

Table 5.2: Runs measured on Mn_4FeSi_3 using the Supernova.

Table 5.3: The unit cell parameters at ambient pressure.

Table 5.4: Test for the different Laue symmetries performed in Jana2006.

Table 5.5: Analysis of the extinction rules of the different hexagonal space groups taken from [Jana2006].

Table 5.6: Structural details for Mn_4FeSi_3

Table 5.7: Symmetry operators of space group $P6_3/mcm$.

Table 5.8: Occupancy parameters (a_i) for the atoms before refinement of the mixed site.

Table 5.9: Atomic coordinates and occupancy parameters in the final refinement.

Table 5.10: Anisotropic displacement parameters [\AA^2] for Mn_4FeSi_3 .

Table 5.11: Equations induced by symmetry.

Table 5.12: Instrumental parameters for the data collection

Table 5.13: Summary of the run list used for the data collection for Mn_4FeSi_3 at all pressure points.

Table 5.14: Details on the structure refinement of Mn_4FeSi_3 for different pressure points.

Chapter 7

Table 7.1: Lattice parameter and unit cell volumes for the different pressure points as extracted from the LeBail refinement.

Table 7.2: Lattice parameter of Mn_4FeSi_3 used for the refinement of the single crystal diffraction data. The parameters were calculated on the basis of the equations of state fitted to the powder diffraction data.

Table 7.3: x-coordinates of Mn2 and Si1 on WP 6g ($x, 0, 1/4$) as a function of pressure.

Table 7.4: Interatomic distances in Mn_4FeSi_3 in [\AA] as a function of pressure.

List of Figures

Chapter 2

Figure 2.1: Schematic representation of a magnetic-refrigeration cycle. The application of the magnetic field leads to an ordering of the magnetic moments. The magnetic entropy is reduced, the lattice entropy is increased and the material heats up. The excess heat is expelled. When the magnetic field is removed, the magnetic moments randomize. The magnetic entropy is increased and the lattice entropy goes down: the temperature of the material drops. Figure from Ref. [Tegus et al, 2002].

Figure 2.2: Magnetic phase diagram showing the different magnetic transitions and phases in the system $Mn_{5-x}Fe_xSi_3$ with $x=0-5$ as a function of temperature [Songlin et al, 2002]. P=paramagnetic, F=ferromagnetic, AF=antiferromagnetic.

Chapter 3

Figure 3.1: A primitive unit cell in the hexagonal system.

Figure 3.2: Illustration of Bragg's law. Two beams with identical wavelength and phase approach a crystalline solid and are scattered by the electron of atoms in two different lattice planes of the crystal. The beam scattered at the lower lattice plane transverses an extra length of $2d\sin\theta$ compared to the beam scattered on the first lattice plane. Constructive interference between both scattered beams can only occur if this length is equal to an integer multiple of the wavelength of the radiation. Figure taken from [Wikipedia, 2015].

Figure 3.3: The Ewald sphere construction taken from [Massa, 2004].

Figure 3.4: Two-dimensional powder diffraction setup with flat plate detector taken from [Klaus-Dieter et al, 2003]

Chapter 4

Figure 4.1: Schematic drawing of an apparatus for cold crucible induction melting. Figure from [Beyss and Gier, 2014].

Figure 4.2: Schematic drawing of an experimental setup for single crystal growth using the Czochralski Method [Gottschlich, 2013].

Figure 4.3: Principle of an X-ray single crystal structure determination.

Figure 4.4: The Agilent Supernova diffractometer at Forschungszentrum Jülich.

Figure 4.5: (a) A schematic representation of a four-circle diffractometer with kappa Geometry taken from [Ladd and Palmer, 2003] (b) Picture of a goniometer head with pin and glass fiber. The crystal is mounted on top of the glass fiber.

Figure 4.6: (a) Boehler-Almax Diamond Anvil Cell made from stainless steel (b) Schematic drawing of the experimental setup in a diamond anvil cell taken from [Yang and Dong, 2011].

Figure 4.7: Parts of a diamond anvil cell and schematic design of the Boehler Almax cell and diamond.

Figure 4.8: The DAC high-pressure chamber containing a sample crystal, a Ruby (pink) and filled with the hydrostatic fluid (blue); on the right the gasket used in this study.

Figure 4.9: Example of the change of the ruby luminescence spectra at two different pressures (ambient and 10 GPa) taken from [Seda, 2005].

Figure 4.10: Photo of the ruby luminescence system available at the RWTH University Aachen used for pressure calibration in the course of this study.

Chapter 5

Figure 5.1: Overview over the steps of a single crystal structure determination.

Figure 5.2: (a) Cylindrical crystal of Mn_4FeSi_3 as prepared with the Czochralski method (b) Small grains of Mn_4FeSi_3 obtained from the large crystal with a hammer (c) a very small crystal magnified by the microscope.

Figure 5.3: (a) Metal pins with glass fibers and sample (b) goniometer head with sample mounted on the diffractometer.

Figure 5.4: Representative frame collected on Mn_4FeSi_3 .

Figure 5.5: Planes of diffracted intensities of Mn_4FeSi_3 with different rotation axis.

Figure 5.6: The single crystal of Mn_4FeSi_3 with the limiting faces.

Figure 5.7: STOEIPDS (Imaging Plate Diffraction System) diffractometer with the mounted diamond anvil cell at the Institute for Crystallography at the Rheinisch-Westfälisch-Technische University in Aachen.

Figure 5.8: Representative frame for the high pressure measurements: Diamond reflection, sample reflection and gasket ring are indicated.

Figure 5.9: (a) Original picture including all found peaks. The brightest lines represent diamond reflections. (b) Picture dominated by reflections from the sample after deleting the diamond reflection. (c) Peaks resulting from the gasket after deleting diamond and sample reflections.

Figure 5.10: Representative frame of Mn_4FeSi_3 . The integration masks are indicated and the masks for the beam stop and the shadowed area of the detector are visible.

Figure 5.11: Screenshot of the graphical interface in the manual culling menu of Jana2006. The x parameter can be changed between four different values ($I(\text{min})$, $I(\text{max})$, $I(\text{average})$ and θ). The y-parameter represents the intensity of the individual reflections $I(i)$ compared with the average intensity $I(\text{average})$ using the value $\Delta = |I(i) - I(\text{average})| / \sigma I(\text{average})$ [Friese, 2013].

Figure 5.12: Detail of the graphical interface in the manual culling menu of Jana2006.

Chapter 6

Figure 6.1: Illustration of the key components of a high-pressure X-ray powder diffraction experiment.

Figure 6.2: a. Beamline ID09A at the European Synchrotron Radiation Facility ESRF, b. The image plate detector Mar555.

Figure 6.3: Stages of data processing of the powder diffraction data. The raw image collected on the Mar555 detector is shown in part (a). The concentric rings correspond to the diffracted intensities from the sample; the bright spot at the upper left corner of the image is an intense diamond reflection from the DAC. These spots have to be masked to avoid contamination of the sample diffraction pattern. Part (b) shows the 1-dimensional pattern obtained by integration with the program FIT2D. The elevated background is due to scattering from the components of the DAC. Part (c) Screenshot of the LeBail-refinement of the data carried out with Jana2006.

Chapter 7

Figure 7. 1: Schematic view of the structure of Mn_4FeSi_3 . Coordination polyhedra around Fe1\Mn1 are indicated.

Figure 7. 2: Schematic view of the structure of Mn_4FeSi_3 along the c-axis. Coordination polyhedra around Fe1\Mn1 and Mn2 are indicated.

Figure 7.3: Pressure dependence of the lattice parameter of Mn_4FeSi_3 . The lattice parameters were extracted from LeBail fits of the powder diffraction measurements performed at ID09A of the ESRF.

Figure 7.4: Pressure dependence of the normalized lattice parameters as extracted from the powder diffraction data measured at beamline ID09A

Figure 7.5: Pressure dependence of the unit-cell volume of Mn_4FeSi_3 . The data are based on synchrotron powder diffraction measurements at Beamline ID09a of the ESRF. Two equations of state were fitted to the data, one for the lower pressure range up to 2 GPa, a second one for the higher pressure range.

Figure 7.6: Pressure dependence of the x coordinate of the Si atom in Mn_4FeSi_3

Figure 7.7: Pressure dependence of the x coordinate of the Mn2 atom in Mn_4FeSi_3

Figure 7.8: Schematic view of the crystal structure of Mn_4FeSi_3 . Mn1/Fe1 atoms are indicated in green, Mn2 atoms in magenta and Si-atoms in blue. Individual distances connecting the atoms are indicated by lines.

Figure 7.9: Pressure dependence of the interatomic distances for Fe1-Mn2, Mn2-Mn2', Mn2-Mn2'', Mn2-Si1, Mn2-Si1'', Si1-Si1''' in Mn_4FeSi_3 .

List of Abbreviations

DAC	Diamond Anvil Cell
<i>GPa</i>	Gigapascal
MCE	Magnetocaloric Effect
ΔT_{ad}	Change in temperature
ΔS_{iso}	Change in entropy
P	Paramagnetic
F	Ferromagnetic
AF	Antiferromagnetic
F_{hkl}	Structure factor
UB	Orientation matrix
CCD	Charge coupled device
ADPs	Atomic displacement parameters
IPDS	Imaging Plate Diffraction System
<i>EMS</i>	Effective Mosaic Spread
EOS	Equation Of State
B_0	Bulk modulus
B'	Pressure derivatives

Chapter 1 Introduction

Magnetocaloric cooling is an energy-efficient and environmentally friendly technology based on the magnetocaloric effect (MCE). Individual compounds in the system $\text{Mn}_{5-x}\text{Fe}_x\text{Si}_3$ ($x=0,1,2,3,4$ and 5) are known as magnetocaloric materials and there are many reports about the crystal structure and magnetic properties of the compounds as a function of temperature [Binczyska et al, 1973; Songlin et al, 2002; Johnson, 1972].

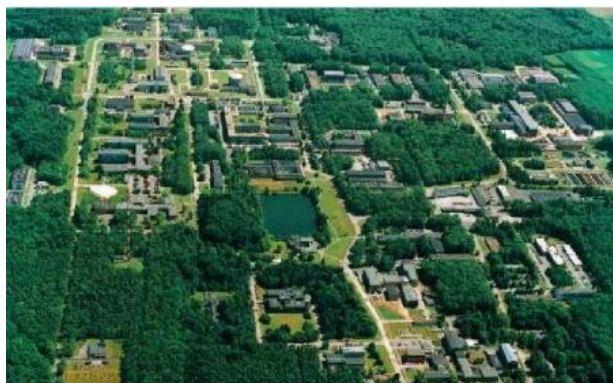
On the other hand, there is little information available on the behavior of the compounds as a function of hydrostatic pressure. Yet the response of the crystal structure to high pressure is of high interest as pressure allows the tuning of the interatomic distances and can thus potentially influence the magnetic phase transitions [Landau, 2007].

In this study, powder and single crystals of MnFe_4Si_3 were synthesized and investigated with X-ray powder and single crystal diffraction in the pressure range from 0.0001 GPa to 6.21 GPa at room temperature. These studies allow the accurate determination of the compressibility and of the structural changes induced by pressure.

1.1 About This Work

Place of research

The experimental work presented in this thesis was performed at the **Jülich Centre for Neutron Science-2 (JCNS)**, the Rheinisch-Westfälisch-Technische Universität Aachen, Germany and the European Synchrotron Radiation Facility (ESRF) in Grenoble, France.



The **Jülich Centre for Neutron Science (JCNS)**, **Research Center Jülich**, develops and operates neutron scattering instruments at several neutron sources worldwide. The in-house research focuses on correlated electron systems and nanomagnetism as well as soft matter and biophysics. Within these areas of expertise, the JCNS offers expert support at

the neutron instruments including specialized sample environment and ancillary laboratory access for external users from science and industry. The Research Centre is located near the town of Jülich, close to the university cities Aachen, Bonn, Cologne and Düsseldorf.

The **Rheinisch Westfälische Technische Hochschule Aachen** is a technical university located in Aachen, North-Rhine-Westphalia, Germany. With more than 42,000 students enrolled in 144 study programs, it is the largest technical university in Germany.

The **European Synchrotron Radiation Facility (ESRF), France**, was inaugurated in 1994 and is a cooperation between 21 partner nations. The ESRF operates more than 40 synchrotron beamlines. Beamline ID09A, where the measurements for this study were carried out, is dedicated to the determination of structural properties of solids at high pressure using angle-dispersive-diffraction in diamond anvil cells.

1.2 Overview of this Research

The overall aim of the work presented in this thesis is to study the effect of hydrostatic pressure on the crystal structure of magnetocaloric Mn_4FeSi_3 .

In chapters two and three the focus is on the motivation and the theoretical background. It includes a detailed discussion of the magneto caloric effect and gives an introduction to the previous work on the compounds in the series $\text{Mn}_{5-x}\text{Fe}_x\text{Si}_3$ ($x=0, 1, 2, 3, 4, 5$). In addition, a description of their crystal structure is included.

Chapter four describes the experimental setups used for the synthesis and the diffraction measurements. A description of the used instruments and the diamond anvil cells (DAC) is also included. **Chapter five** presents an overview of the experimental procedures needed for the determination of the crystal structure of Mn_4FeSi_3 at ambient pressure and high pressure from single crystal diffraction data.

Chapter six reviews the high-pressure powder diffraction techniques. **Chapter seven** summarizes the results of the experimental work. The data for the different pressure points is presented and the effect of pressure on the crystal structure of Mn_4FeSi_3 is described. Finally, **Chapter eight** provides conclusions and includes recommendations for future work.

Chapter 2 Background

2.1 The Magneto caloric Effect

The magnetocaloric effect (MCE) is the change of the temperature of a magnetic material as a response to the application of a magnetic field. The magnetocaloric effect can be characterized in two ways: the change in temperature (ΔT_{ad}) in an adiabatic process or the change in entropy (ΔS_{iso}) in an isothermal process.

The magnetocaloric effect can be used as the basis for magneto caloric refrigeration which is an environmentally friendly technology [Oliveira et al, 2002]. A schematic representation of the magnetocaloric refrigeration cycle is shown in (figure 2.1). When a magnetic field is applied to a paramagnetic material, the magnetic moments in the material order, this way causing a reduction in total entropy. As a consequence, to keep the total entropy in the adiabatic process constant, the crystalline lattice entropy should increase, and, as a result of this, the material heats up. The excess heat can then be expelled. If the magnetic field is then adiabatically removed, the spins disorder again causing an increase in total entropy. To keep the total entropy constant the lattice entropy has to be reduced and, as a consequence, the material cools down.

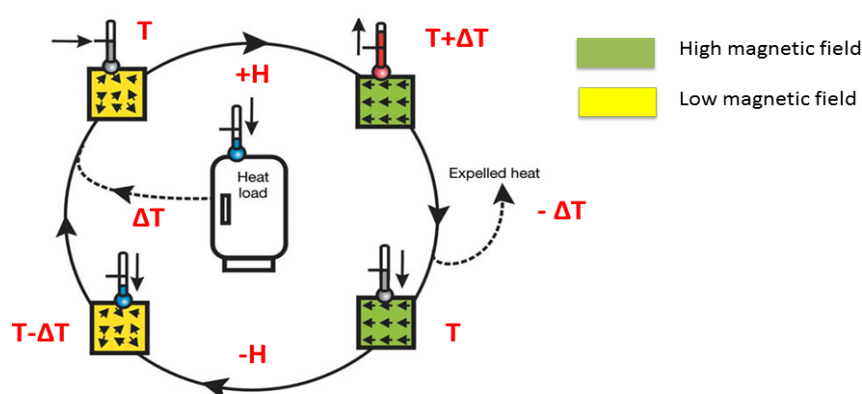


Figure 2.1: Schematic representation of a magnetic-refrigeration cycle. The application of the magnetic field leads to an ordering of the magnetic moments. The magnetic entropy is reduced, the lattice entropy is increased and the material heats up. The excess heat is expelled. When the magnetic field is removed, the magnetic moments randomize. The magnetic entropy is increased and the lattice entropy goes down: the temperature of the material drops. Figure from Ref.[Tegus et al, 2002].

2.2 Previous work on compounds of the series $Mn_{5-x}Fe_xSi_3$ ($x=0-5$)

The magnetic and magnetocaloric properties of the compounds in the system $Mn_{5-x}Fe_xSi_3$ ($x=0-5$) have been investigated by measuring the magnetization as a function of

temperature and magnetic field [Songlin et al, 2002]. Depending on the temperature and the composition different magnetic phases have been found. The information on them is summarized in the magnetic phase diagram (Figure 2.2).

As can be seen for the Mn-rich compounds in the system ($x=0,1,2,3$) two different antiferromagnetic phases are observed while for the Fe-rich members of the series ($x=4,5$) ferromagnetic ordering is observed. The compound Mn_4FeSi_3 ($x=1$), which is studied in this thesis has two magnetic phase transitions as a function of temperature. At 95 K the paramagnetic phase converts to a collinear antiferromagnetic phase AF2 and at 65K the collinear antiferromagnetic phase undergoes a transition to a second antiferromagnetic phase with anon-collinear spin arrangement. [Candini et al, 2004; Songlin et al, 2002].

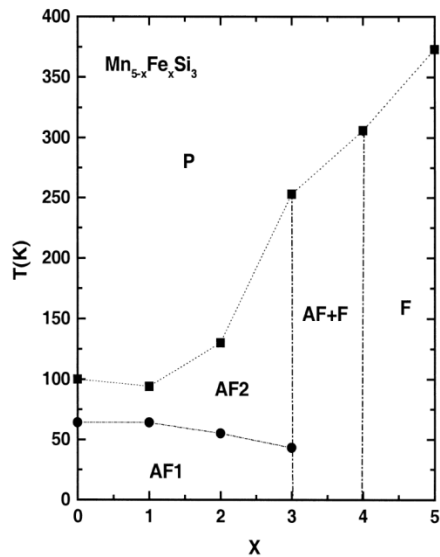


Figure 2.2: Magnetic phase diagram showing the different magnetic transitions and phases in the system $Mn_{5-x}Fe_xSi_3$ with $x=0-5$ as a function of temperature [Songlin et al, 2002]. P=paramagnetic, F=ferromagnetic, AF=antiferromagnetic.

Chapter 3 Theoretical Concepts

The aim of this thesis was to characterize the influence of hydrostatic pressure on the crystal structure of Mn_4FeSi_3 by means of single crystal x-ray diffraction. In particular, we wanted to answer the question whether the application of chemical pressure (through the incorporation of smaller Fe-atoms in the structure) and of hydrostatic pressure lead to similar changes in the crystal structure.

3.1 Some Basic Concepts of Crystallography

A crystal is formed from an ordered arrangement of atoms, molecules, or ions. The crystal lattice is characterized by three lattice parameters (a, b, c) and the angles between them (α, β, γ), which define the unit cell of the crystal. Crystal structures are characterized by their specific symmetries. The observed symmetry elements (mirror- or glide-planes, rotation or root-inversion axis, inversion centers) within a crystal structure determine the crystal system and can force certain lattice parameters a, b, c to be equal or force the angles α, β, γ to have special values (90° or 120°). In a diffraction experiment the symmetry operations imply that certain symmetry equivalent reflections have identical intensities.

All lattices can be classified in seven crystal systems. Depending on how many lattice points exist in the unit cell and where they are situated, these lattices are classified as primitive (P), body-centered (I), face-centered (F), base-centered A, B, or C. The symmetry of an object is expressed by point group symmetry; the symmetry of a crystal structure is expressed by a space group symmetry. The 230 space groups result from the combination of the symmetry elements with translational symmetry. The *Laue group* is the symmetry of a diffraction pattern and can be determined from the observed intensities. As in a x-ray diffraction experiment (in the absence of resonant scattering) a center of inversion is added to the point group symmetry, Laue groups are always centrosymmetric.

The compounds investigated in this thesis crystallize in the hexagonal system where a and b lattice parameters are equal and enclose an angle of $\gamma=120^\circ$. The c -lattice parameter is different from a and b and the angles α and β between c and a (or b) are 90° . The hexagonal crystal system has only one Bravais lattice type: simple (P). A sketch of the unit cell is shown in (figure 3.1).

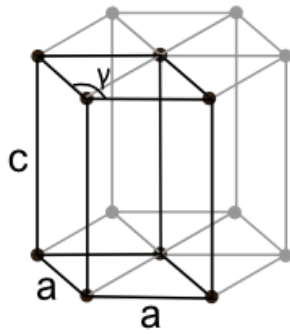


Figure 3.1: A primitive unit cell in the hexagonal system.

3.2 X-Ray Diffraction and Bragg's Law

X-rays were discovered in 1895 by the German physicist Roentgen [Röntgen, 1895]. Diffraction from a crystal lattice has first been observed and interpreted by Max von Laue [Laue, 1912; Friedrich, 1912]. Diffraction arises from the interference of scattered photons, which are produced by the elastic scattering of incident electromagnetic radiation by the electrons of the atoms within a crystal lattice. X-ray diffraction is a standard method to determine the structure of crystalline solids and allows to determine the atomic positions within a crystalline solid. Yet it can also be used for quantitative phase analysis, for stress measurements and /or, to study phase equilibrium or for the measurement of particle sizes. X-ray diffraction techniques can be used on single crystals, polycrystalline materials, thin films or nanoparticles. The condition for diffraction can be defined mathematically by Bragg's law or geometrically by the Ewald sphere construction, in real or reciprocal space, respectively.

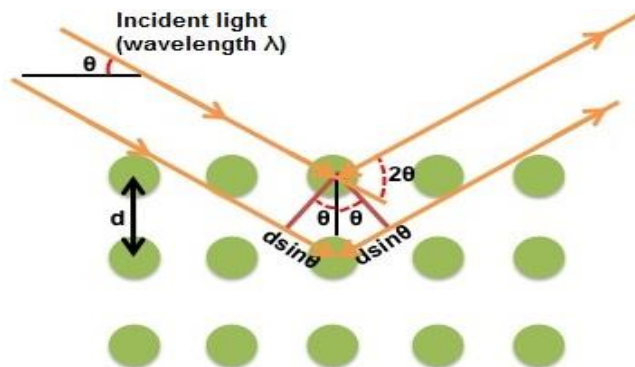


Figure 3.2: Illustration of Bragg's law. Two beams with identical wavelength and phase approach a crystalline solid and are scattered by the electron of atoms in two different lattice planes of the crystal. The beam scattered at the lower lattice plane transverse an extra length of $2d\sin\theta$ compared to the beam scattered on the first lattice plane. Constructive interference between both scattered beams can only occur if this length is equal to an integer multiple of the wavelength of the radiation. Figure taken from [Wikipedia, 2015].

The basic principle of x-ray diffraction is described in Bragg's law. In the crystal the atoms are associated with a set of evenly spaced lattice planes with spacing's comparable

to the wavelength of the incoming x-ray beam. Each set of lattice planes in the crystal is characterized by its corresponding Miller indices (hkl).

If a beam of wavelength λ hits a lattice plane (hkl) under an angle θ it is scattered under an identical angle θ (figure 3.1.). If a second beam with identical phase is scattered by an atom in another parallel lattice plane (hkl) then it transverses an extra length of $2d\sin\theta$. Constructive interference between both scattered beams can only occur if this extra length is a multiple of the wavelength of the x-ray beam. This is expressed by Bragg's law

$$n\lambda = 2d_{hkl}\sin\theta \quad 3.1$$

3.3 Ewald Sphere Construction

The Ewald sphere construction [Ewald, 1913] is shown in (Figure 3.2). It is a geometrical operation applied to a reciprocal lattice in order to explore the diffraction characteristics exhibited by a crystal. The sphere has a radius of $1/\lambda$ where λ is the wavelength of the incoming x-ray beam. The origin of real space of the crystal is at the center of the Ewald sphere. The origin of reciprocal space is on the intersection of the Ewald sphere with the incoming x-ray beam. Any rotation of the crystal in real space leads to a rotation of the reciprocal lattice around its origin. The angle between the incident and diffracted beams is 2θ and the vector connecting the reciprocal space origin and the diffraction point is the diffraction vector \mathbf{d}^* .

The validity of the Bragg equation for a lattice plane with spacing d thus implies that the corresponding scattering vector \mathbf{d}^* must lie on a circle with radius $1/\lambda$ about \mathbf{K} . Visualization of the Ewald sphere construction is an easy way to understand which points of the reciprocal lattice fulfill the diffraction condition.

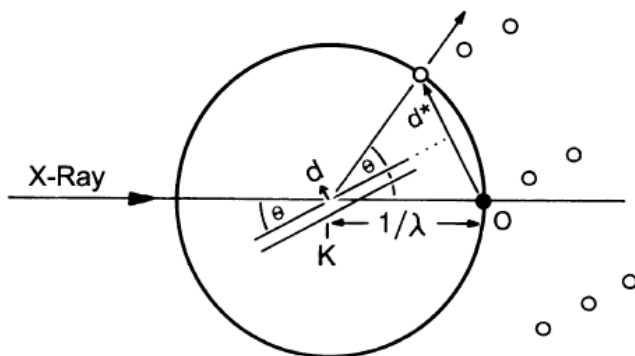


Figure 3.3: The Ewald sphere construction taken from [Massa, 2004]

3.4 X-Ray Powder Diffraction

X-ray powder diffraction may be considered as diffraction on a series of randomly oriented crystallites. This situation results in concentric cones of diffracted intensity emanating from the sample position as shown in (Figure 3.4). These would then appear as a series of concentric rings on an detector placed normal to the X-ray beam. The 2-dimensional diffraction images can then be integrated to produce a one-dimensional plot of intensity against diffraction angle (2θ). The quality of the powder diffraction pattern is usually limited by the nature and the energy of the available radiation, by the quality of the sample and by other effects like e.g. decent ring of the sample. More details concerning the powder diffraction experiments which were carried out are given in **chapter6**.

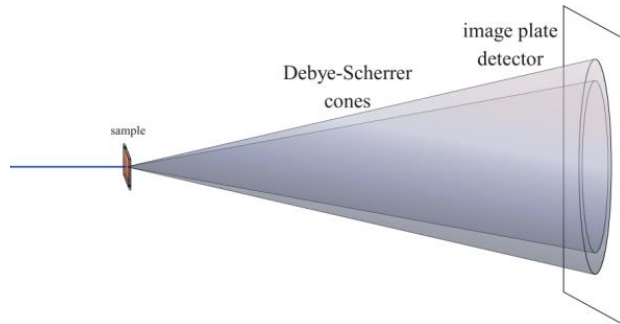


Figure 3.4: Two-dimensional powder diffraction setup with flat plate detector taken from [Klaus-Dieter et al, 2003].

3.5 The Structure Factor

The structure factor depends on the distribution of the different atoms within the unit cell of the crystal. It can be expressed in terms of the contents of a single unit cell as:

$$F_{hkl} = \sum_{j=1}^N f_j e^{2\pi i(hx_j + ky_j + lz_j)} \quad 3.2$$

where the sum is over all the atoms j in the unit cell; f_j is the atomic scattering factor of atom j ; x_j , y_j and z_j are the coordinates of atom j in the three directions and hkl are the Miller indices of the respective lattice planes. The structure-factor equation is the basis for crystal structure determination. It plays a central role in the solution and refinement of crystal structures as the square of the structure factor is proportional to the observed diffracted intensity:

$$I_{hkl} \approx |F_{hkl}|^2$$

The set of structure factors for all the reflections hkl are the primary quantities necessary for the derivation of the three-dimensional distribution of electron density.

3.5.1 The phase problem of X-ray crystallography

The phase problem is a basic problem in x-ray crystallography. When a crystal is exposed to a beam of X-rays, the resulting interference effect gives rise to the so-called diffraction pattern. The x-ray detector can only record intensities but not the phases of the electromagnetic waves. Each reflection on the diffraction pattern corresponds to a wave consisting of an amplitude and a phase. The amplitude is easily calculated by taking the square root of the intensity, but the information about the phase is lost. However, owing to the known atomicity of real structures and the large number of observable intensities, the lost phase information can be recovered from the measured intensities using specific and well-developed algorithms. The problem of recovering the missing phases, when only the intensities are available, is known as the phase problem. Alternatively, since the magnitudes $|F_{hkl}|$ of the normalized structure factors

$$F_{hkl} = |F_{hkl}| \exp(i\phi_{hkl})$$

Can be directly determined from the measured diffraction intensities, the phase problem may be defined as the problem of determining the phases ϕ_{hkl} when the magnitudes $|F_{hkl}|$ are given.

Chapter 4 Experimental Techniques

This chapter presents an overview of the experimental techniques and the instruments used in this study. At first the synthesis method is described. Then the use of single crystal diffraction at ambient pressure using the Supernova diffractometer based in the Jülich Center for Neutron Science in Jülich is discussed, and in the next section single crystal diffraction experiments under high pressure using a diamond anvil cell in combination with a STOE IPDS diffractometer at the Institute for Crystallography at the Rheinisch-Westfälische Technische Universität in Aachen are described.

4.1 Synthesis of the Single Crystal of $Mn_{5-x}Fe_xSi_3$ with $x=1$

The compound Mn_4FeSi_3 is one of the compounds in the series $Mn_{5-x}Fe_xSi_3$. The crystal structure of the compounds in this system was reported by Binczycka [Binczycka et al, 1973]. Polycrystalline samples have been prepared previously in laboratories at the Forschungszentrum Jülich. They were prepared by inductive melting using a cold crucible [Jouan, 1996]. A schematic drawing of the apparatus is shown in (Figure 4.1).

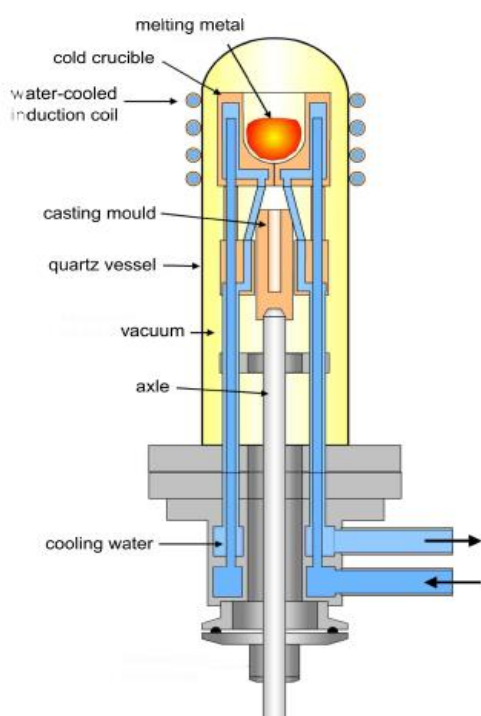


Figure 4.1: Schematic drawing of an apparatus for cold crucible induction melting. Figure from [Beys and Gier, 2014].

For the synthesis the elements Mn and Fe, Si were weighted in stoichiometric relationship. They were put in a water-cooled copper crucible and melted with high

frequency alternating magnetic fields. The crucible is surrounded by induction coils and consists of several segments which allow the generation of an induced current in the metal and the creation of the magnetic field in the metallic sample. The metal is melted by Joule heating caused by eddy currents.

The polycrystalline samples synthesized this way were used as starting materials for the growth of a large single crystal of Mn_4FeSi_3 . For this, the Czochralski technique (1918) [Czochralski, 1918] was used at the Forschungszentrum Jülich. A scheme of the experimental setup is presented in (Figure 4.2). The starting material is placed in a crucible and heated up till a melt is produced. A small seed crystal is lowered into the melt and the crystallization process starts on the surface of this small crystal seed.

The seed is mounted on the lower tip of a water cooled rod. The rod with the seed is dipped into the melt and then starts to move up with a velocity of 15mm per hour. At the same time the rod with the solidified crystal is rotating and a crystal is grown in the shape of a cylinder.

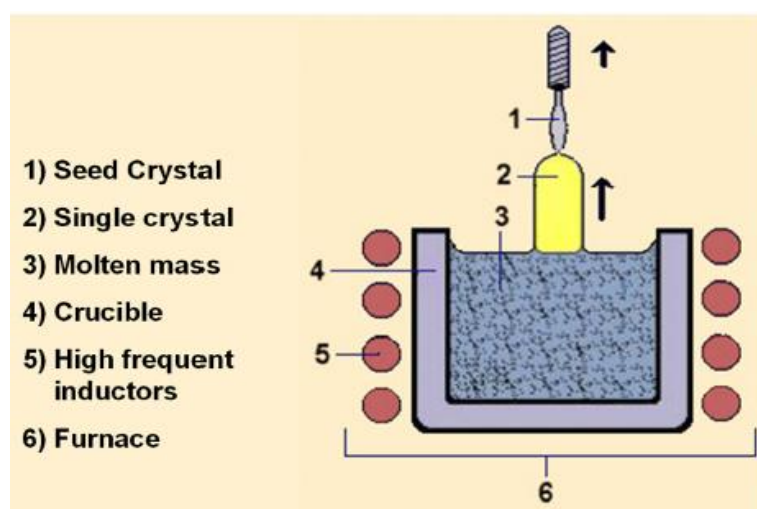


Figure 4.2: Schematic drawing of an experimental setup for single crystal growth using the Czochralski Method [Drawing from Gottschlich, 2013]

4.2 Single Crystal X-ray Crystallography

Single crystal X-ray crystallography is a non-destructive analytical technique [xray.chem, 2010] and is a well-established and very precise method, which provides detailed information about a crystal structure. A crystal is put on a goniometer and gradually rotated to different angles while a beam of X-rays bombards the crystal. Whenever the Bragg equation is fulfilled, scattered beams are produced, and on a detector these scattered beams result in a diffraction pattern composed of spots which are called

reflections. From the angles and intensities of these diffracted beams, the three dimensional electron density distribution within the unit cell of the crystal can be reproduced using complex data analysis routines which are based on Fourier transforms as shown in (Figure 4.3).

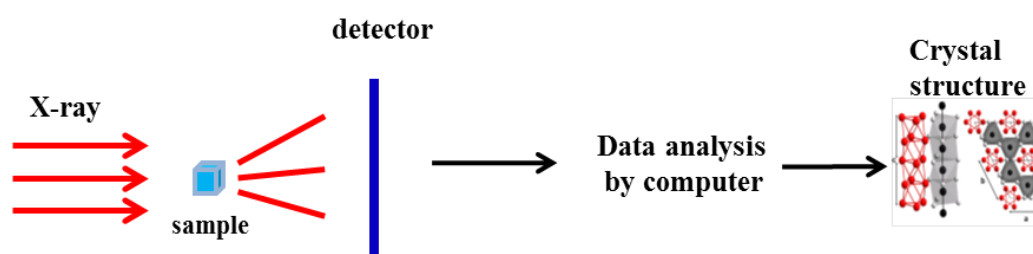


Figure 4.3: Principle of an X-ray single crystal structure determination.

4.2.1 Single Crystal Diffraction at Ambient Pressure

In this study an Agilent Technologies “Supernova” 4-circle diffractometer at Forschungszentrum Jülich was used for recording the diffraction intensities of Mn_4FeSi_3 at ambient pressure and temperature (Figure 4.4).



Figure 4.4: The Agilent Supernova diffractometer at Forschungszentrum Jülich

The Supernova diffractometer consists of a micro focus X-ray tube (both $\text{MoK}\alpha$ and $\text{CuK}\alpha$ radiation are available) typically operated at 40 kV/1.5 mA, which is combined with a multilayer X-ray optics to obtain increased intensity and monochromatic $\text{K}\alpha_1 / \text{K}\alpha_2$ radiation. The single crystal “Supernova” diffractometer is a 4-circle diffractometer with kappa geometry. All the axes of the four circles of the diffractometer, κ (kappa), ω , Φ and 2θ , intersect in the center of the diffractometer.

The crystal is mounted on a small glass pin and fixed to a goniometer head which in turn is placed on the diffractometer as shown in figure 4.5a. With the help of the centering screws of the goniometer head it is possible to keep the crystal at the center of the diffractometer throughout the data collection.

The goniometer head is mounted on the Φ -axis, which is placed on the κ -block. The κ -block is rotated about the κ -axis, being itself carried by the ω -block. The axis of the "circle", is tilted by 50° out of the horizontal plane. The ω -block is rotated about the axis (ω_κ) and serves as the diffractometer base. The 2θ -axis, which coincides with the ω -axis, carries the CCD detector, (Figure 4.5(b)).

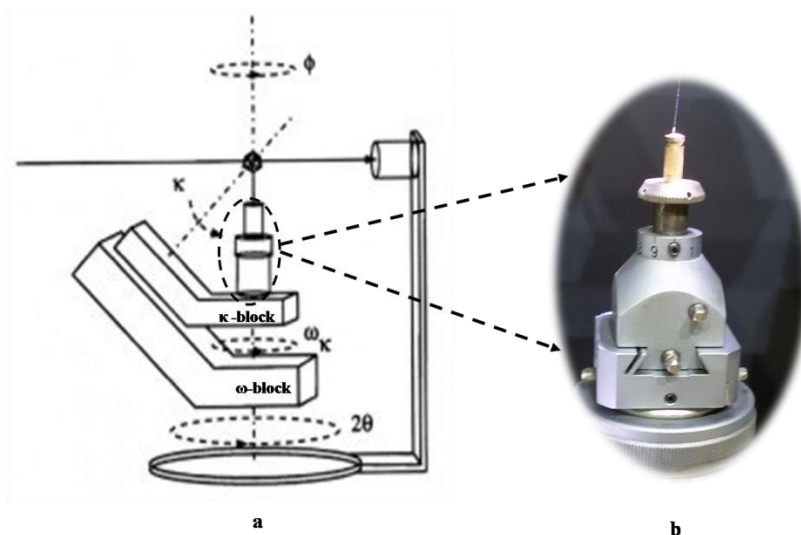


Figure 4.5: (a) A schematic representation of a four-circle diffractometer with kappa Geometry taken from [Ladd and Palmer, 2003] (b) Picture of a goniometer head with pin and glass fiber. The crystal is mounted on top of the glass fiber.

A Charge Coupled Device (CCD)-system is used to record the data on the "Supernova" diffractometer. The reflections can be recorded very quickly almost in real time and a high efficiency is achieved through the use of a special grade phosphor (Gd_2O_2S) with directly bonded high-quality fiber optics [Ladd and Palmer, 2003]. The level of background noise is reduced by cooling the chip with a Peltier element to between 40 and $60^\circ C$ [Massa, 2004]. The diffractometer can be combined with a low-temperature Oxford Cryostream system which operates in the temperature range from 80 - 500 K.

4.3 Single Crystal Diffraction Under High Pressure

The X-ray diffraction experiments described in the former chapter, allow to characterize the crystal structure of Mn_4FeSi_3 at ambient conditions. To better understand the structural stability, it is useful to use different conditions, e.g., to change the pressure or the temperature.

Therefore, to observe the change of the crystal structure of Mn_4FeSi_3 under the application of hydrostatic pressure, in situ single crystal diffraction experiments using a diamond anvil cell were carried out.

4.3.1 The diamond anvil cell (DAC)

The DAC is a powerful device to generate every high static pressures and thus allows the discovery of new states of matter. The main components of a DAC that determine which maximum hydrostatic pressures can be reached in an experiment are the shape and the size of the diamonds, the hardness of the material which forms the cell body, the gasket material which is used to confine the sample and the used pressure medium. Pressure calibration is done with the ruby luminescence method [Forman et al, 1972, Mao and Bell, 1979].

In the diamond anvil cell used in the course of this study a gasket is placed between two diamond anvils which are mounted on stainless steel backing plates as shown in figure 4.6a. A hole is drilled into the gasket and the sample is placed into the hole together with a pressure transmitting medium. The diamonds are then pushed together and the pressure medium converts the uniaxial pressure exerted by the diamonds to hydrostatic pressure as shown in (Figure 4.6(b)).

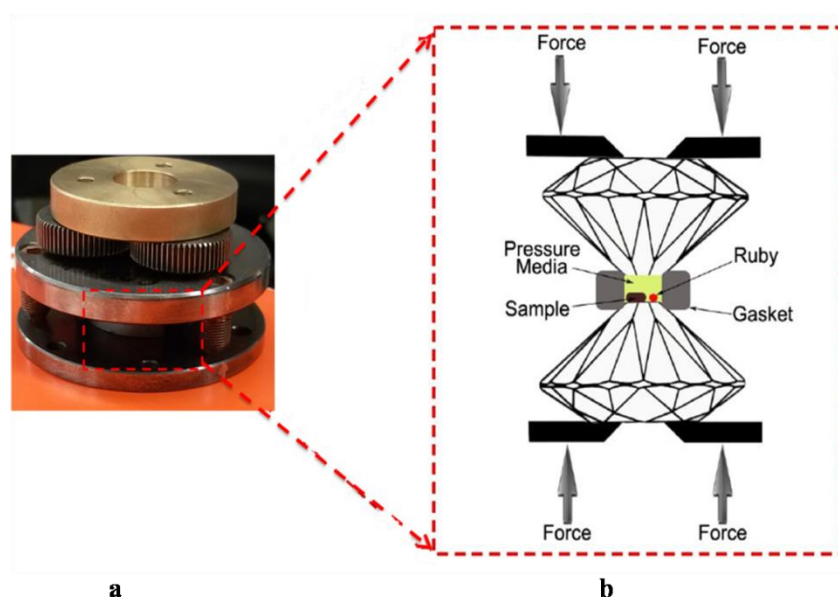


Figure 4.6: (a) Boehler-Almax Diamond Anvil Cell made from stainless steel (b) Schematic drawing of the experimental setup in a diamond anvil cell taken from [Yang and Dong, 2011].

The performance of a DAC depends critically on the composition, size and shape of the diamonds which are used. Diamonds with large culet diameter are generally limited to lower pressures and diamonds with small culet diameter are needed for larger pressures.

As diamonds are very hard materials and very resistant to heat and scratching they are ideally suited for high pressure experiments. The diamonds used in DAC are generally of natural origin and cut according to the brilliant-cut. A further advantage of the diamonds

is that they are transparent to many kinds of electromagnetic radiation, e.g. gamma rays. In addition, they have relatively low absorption coefficients for X-rays (e.g. $\mu(\text{MoK}\alpha)=0.202 \text{ mm}^{-1}$ [Katrusiak, 2008] and thus allow the incoming and scattered beams in a diffraction experiment to pass through them.

The diamond anvil cell used in this experiment is of the Boehler-Almax type [Boehler, 2006]. The culet size was 600 μm which allows reaching a maximum pressure of approx. 10.0 GPa. As a pressure mechanism a "screw drive" is used which applies pressure to the outer faces of the diamonds by tightening three screws in the steel body, as shown in (Figure 4.7).

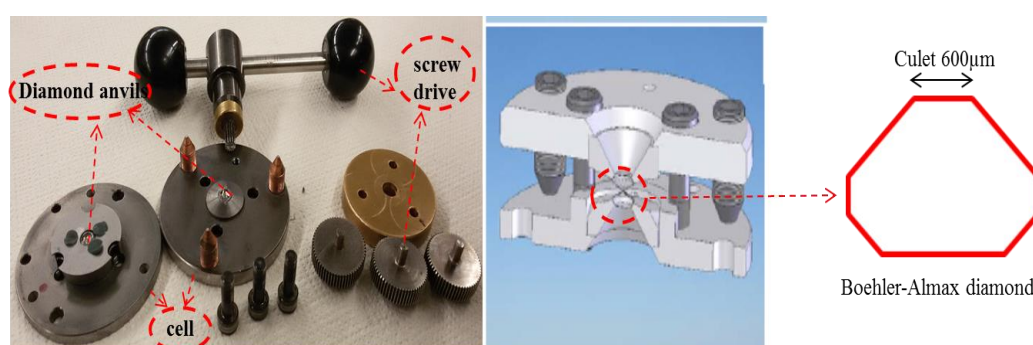


Figure 4.7: Parts of a diamond anvil cell and schematic design of the Boehler Almax cell and diamond.

The use of a metal gasket in a DAC for the confinement of the pressure medium was first introduced by Van Valkenburg [Valkenburg, 1962] and since then has been widely used. Gaskets are made from different types of material like e.g. steel, rhenium, tungsten, or beryllium. For the experiments in this study the gaskets were composed of stainless steel. The gasket extrudes around the diamonds and acts as a supporting ring for the diamond culets. This lateral support of the culets by the gasket reduces the edge chipping of diamonds.

The initial thickness of the commercially available gaskets is approximately 250 μm . Before the experiments the gaskets are preindented to a thickness between 150 to 100 μm . For the diamond anvil cell equipped with diamonds of 600 μm culet a hole of 300 μm was drilled at the center of the preindentation. The sample, a ruby chip and the pressure medium were placed in the hole of the gaskets shown in (Figure 4.8).

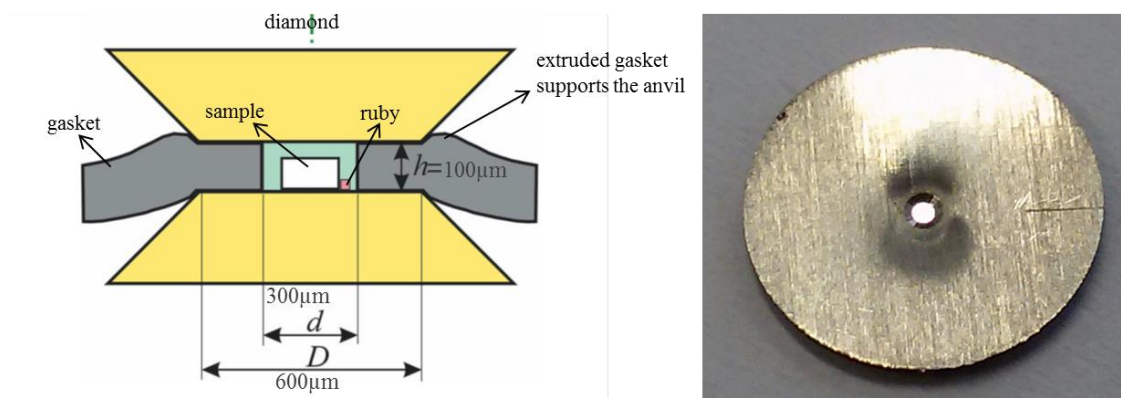


Figure 4.8: The DAC high-pressure chamber containing a sample crystal, a Ruby (pink) and filled with the hydrostatic fluid (blue); on the right the gasket used in this study.

The main objective of the pressure medium is to convert the uniaxial pressure exerted by the diamonds to hydrostatic pressure on the sample. Various fluids have been reported to be good hydrostatic pressure transmitting media, yet all pressure media only ensure hydrostatic conditions up to a limiting value. The hydrostatic limits of many organic fluid pressure media were determined earlier [**Piermarini and Barnett, 1976**].

In the experiment the pressure medium is placed into the gasket hole together with the sample and the ruby chips and the DAC is then closed. The sample and the ruby($\text{Al}_2\text{O}_3:\text{Cr}$) in the gasket hole are this way completely surrounded by a fluid. In the experiments described here a mixture of 4:1 methanol-ethanol, which is found to remain hydrostatic up to 10 GPa at room temperature, was used as a pressure transmitting medium [**Piermarini and Barnett, 1976**].

4.3.2 Pressure measurements with ruby fluorescence

The standard method to measure pressure in a diamond anvil cell is by measuring the shift of the lines in the luminescence spectra of ruby. This method was first used by **Piermarini et Al.** and later on further established by **Bell & Mao** [**Forman et al, 1972; Mao and Bell, 1979**]. Within a small chip (8-12 μm) of ruby($\text{Al}_2\text{O}_3:\text{Cr}$) which is enclosed in the sample chamber the luminescence lines R1 and R2 of ruby are excited with a laser. The doublet R1 and R2 have sharp lines at wavelengths of ~694.2 nm and ~692.7 nm, respectively, at ambient conditions. Under pressure, these lines shift to higher wavelengths as shown in (Figure 4.9). From the shift of the lines the pressure in the DAC can be deduced. The ruby luminescence system used in the course of this study is shown in (Figure 4.10).

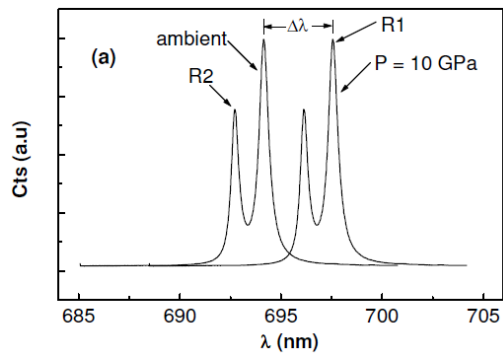


Figure 4.9: Example of the change of the ruby luminescence spectra at two different pressures (ambient and 10 GPa) taken from [Seda, 2005].

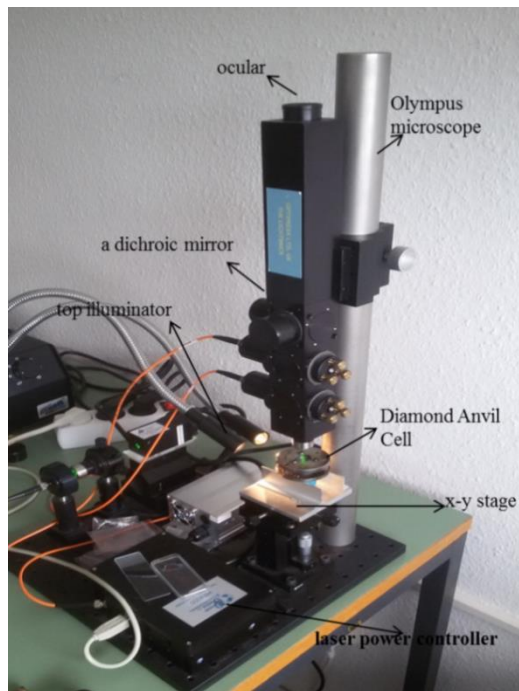


Figure 4.10: Photo of the ruby luminescence system available at the RWTH University Aachen used for pressure calibration in the course of this study.

Chapter 5 Experimental Procedures

This chapter presents an overview of the experimental procedures followed for the determination of the single crystal structure of Mn_4FeSi_3 at ambient pressure and high pressure.

5.1 Single Crystal Structure Determination at Ambient Pressure

A successful X-ray single crystal structure determination consists of several steps as shown in (Figure 5.1). First, an appropriate single crystal of adequate size and very good quality has to be chosen on the basis of optical characteristics. The crystal is then glued on a glass fiber and mounted on a goniometer head. The diffraction intensities of the crystal are then measured using a single crystal diffractometer by rotating the crystal around the pertinent axis while recording the intensities simultaneously on a 2-dimensional detector. Once the measurement is finished a search for peaks which exceed a certain intensity level is performed. The peaks are subsequently indexed using the algorithm implemented in the diffractometer software. Once a reliable orientation matrix has been obtained, the intensities of the individual reflections are integrated which are subsequently corrected for several effects (Lorentz-Polarization, absorption).

As an outcome of the integration one obtains a file containing the integrated intensities of the reflections h,k,l together with an estimation of their standard deviation. In the next step one needs an initial model of the crystal structure. This can be either obtained by structure solution methods (like Patterson or Direct Methods) or the structural model can be deduced from literature data of similar compounds. For the structure refinements of Mn_4FeSi_3 we used the model published by [Binczyska et al, 1973].

In the structure refinement process the structure factors calculated on the basis of the initial model are compared to the observed values and their differences are minimized in a least square process in which the structural parameters like atomic coordinates and displacement parameters are varied. In the final structure refinement the differences between observed and calculated values are minimal and a structural model including the atomic coordinates and displacement parameters is obtained.

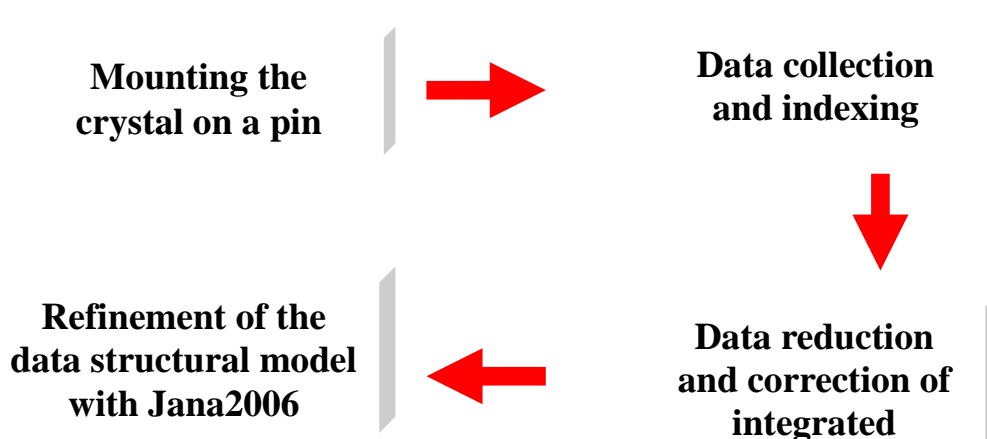


Figure 5.1: Overview over the steps of a single crystal structure determination.

5.1.1 Crystal selection

The precision and quality of a crystal structure determination depends on the quality of the crystal as one of the most important factors. When the choice of the sample is appropriate, the data quality will be very good and the errors in the following steps will be minimal. As a consequence the integrated intensities after data reduction will be very precise.

A good crystal should not be twinned and should not have any small crystallites glued to it, as this would influence the data quality. Well-developed natural faces are in general indicators of high quality. The crystal should be smaller than the x-ray beam to ensure that the diffracting volume is constant during the whole measurement.

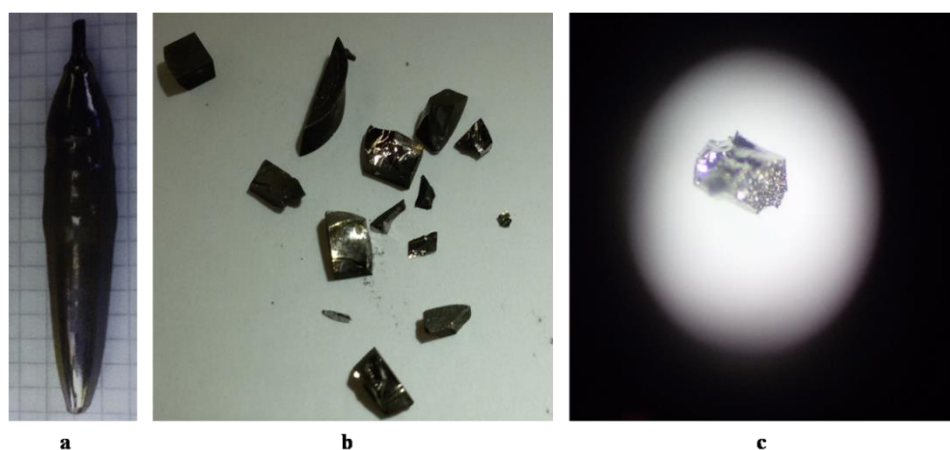


Figure 5.2: (a) Cylindrical crystal of Mn_4FeSi_3 as prepared with the Czochralski method (b) Small grains of Mn_4FeSi_3 obtained from the large crystal with a hammer (c) a very small crystal magnified by the microscope.

The initial crystal prepared with the Czochralski method had a cylindrical shape as shown in (Figure 5.2(a)). The large crystal of Mn_4FeSi_3 was broken into smaller grains Figure 5.2(b) and a single crystal for the diffraction measurement was selected using an optical

microscope (magnification x40). The dimension of the measured single crystal of Mn_4FeSi_3 was $0.014 \times 0.053 \times 0.032$ mm. Polarized light was used to check for uniform optical extinction. This way the quality of the crystal was additionally checked as shown in Figure 5.2(c).

5.1.2 Mounting the sample

After choosing appropriate crystals they are glued on top of a glass fiber which in turn is mounted onto a small metal pin. The top glass fiber should be very thin and well adapted to the sample size. The basic procedure followed for mounting the crystal was:

1. Enter the glass fiber into a copper metal pin and fix it with glue (Figure 5.3a).
2. Select a suitable crystal which fits the size of the glass fiber, put a little bit of glue on top of the fiber and glue the crystal to it under the microscope. Mount the metal pin with the crystal onto a goniometer head
3. Attach the goniometer head to the ϕ circle of the diffractometer (Figure 5.3b).

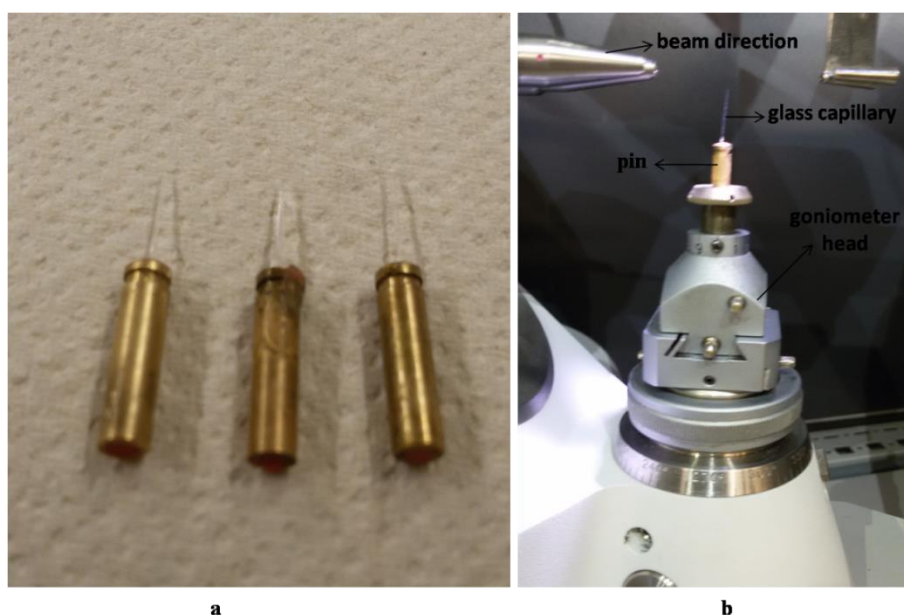


Figure 5.3(a) Metal pins with glass fibers and sample (b)goniometer head with sample mounted on the diffractometer

Crystal alignment

Once the crystal is on the diffractometer (a Supernova 4-circle diffractometer with κ -geometry from Agilent) it has to be optically adjusted so that its center does not move when it is rotated. The sample was aligned using a dedicated video microscope of 120x magnification and sample illumination provided by focusing LEDs mounted aside the beam stop of the system [Perlan, 2010]. The crystal is centered in X and Y by checking its

position at angles $\varphi = 0, 90, 180$ and 270° and then the height Z is adjusted. The height Z was checked at two different κ -values ($\kappa = -90$ and $+90^\circ$).

5.1.3 Search for reflections

Once the crystal is mounted and properly centered it is exposed to an intense beam of X-rays. With the CrysAlis^{PRO} software the 4-circles κ (kappa), ω , φ and 2θ (see section 4.2.1) can be controlled and the crystal can be oriented relative to the incident X-ray beam so that the Bragg condition is met. The crystal is rotated step-by-step through different angles (κ, ω, φ), where φ represents the rotation of the sample about the vertical axis of the goniometer head, ω concerns the rotation of the base of the diffractometer about its physical vertical axis, and κ is the motor that provides vertical tilt of the goniometer head.

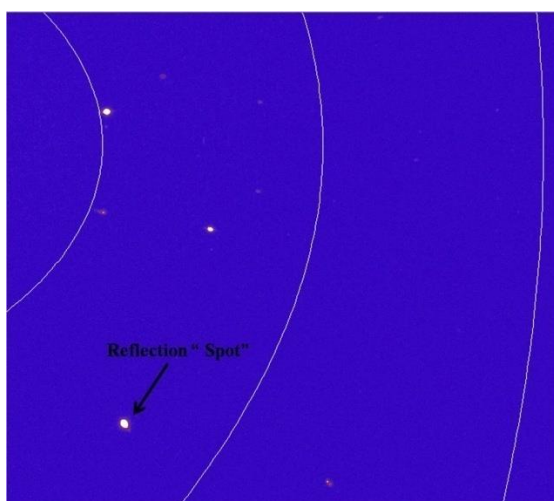


Figure 5.4: Representative frame collected on MnFe_4Si_3

During the rotations the reflections are recorded with a charge-coupled device (CCD) image sensor (Figure 5.4). The rotations are required to cover all of reciprocal space. The rotation axis should be changed at least once, to avoid developing a "blind spot" in reciprocal space close to the rotation axis (Figure 5.5).

This way a large number of reflection intensities are recorded. The position of the resulting diffraction intensities is related to the shape and orientation of the unit cell of the crystal while the relative intensities provide the information on the position and thermal movement of the atoms in the unit cell. Parameters defining the individual data collection for the experiment on Mn_4FeSi_3 are shown in (Table 5.1) and (Table 5.2) gives the details of different runs and measurements for Mn_4FeSi_3 .

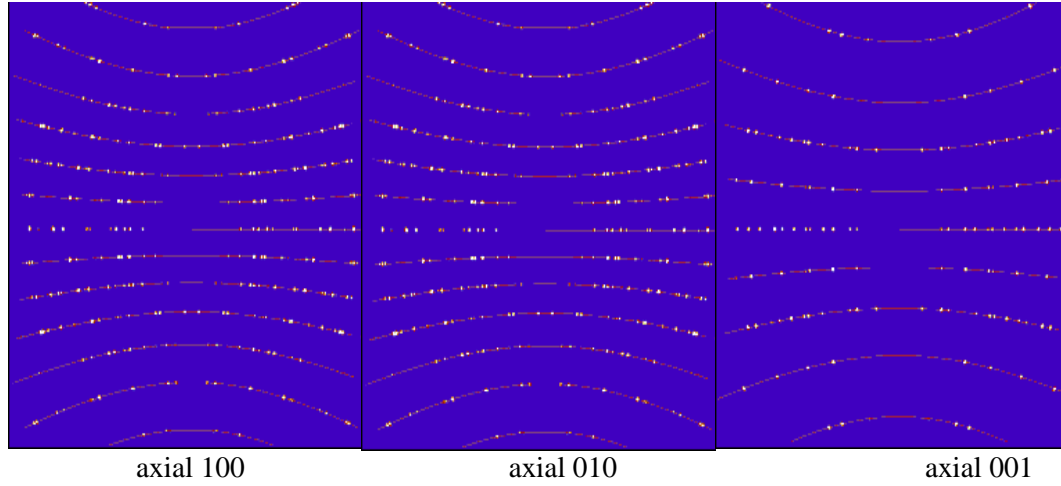


Figure 5.5: Planes of diffracted intensities of Mn_4FeSi_3 with different rotation axis

Wavelength	Mo
Voltage	50.00kV
Current	0.80mA
Detector distance	55.66mm
omega scans	21runs; 1175 total number of frames
Scan width	1.000°
Exposure time	7.76s
Total data collection time	6h 39m 52s

Table 5.1: Data collection parameters for the measurement on Mn_4FeSi_3 at ambient conditions

Run #	ω_k start	ω_k End	θ	K	Φ	# of Frames	# of Reflections
Run 1	-11.000	16.00	24.00	82.00	-43.4	27	169
Run 2	-33.000	-7.00	-44.00	-88.00	139.20	26	238
Run 3	-40.000	-15.00	-48.00	-83.00	15.95	25	246
Run 4	-41.000	-15.00	-49.94	-82.00	47.13	26	276
Run 5	-56.000	21.00	-49.94	77.00	90.00	77	823
Run 6	-44.000	-18.00	-49.94	-81.00	132.56	26	275
Run 7	-42.000	-16.00	-49.94	-80.00	-22.61	26	273
Run 8	-44.000	-16.00	-49.94	-80.00	-136.19	28	299
Run 9	87.000	114.00	50.87	125.00	-180.00	27	291
Run 10	24.000	104.00	50.87	57.00	150.00	80	883
Run 11	-25.000	52.00	50.87	-38.00	-180.00	77	840
Run 12	2.000	95.00	50.87	-125.0	60.00	93	1020
Run 13	32.000	107.00	50.87	38.00	-120.00	75	816
Run 14	23.000	121.00	50.87	57.00	30.000	98	1068
Run 15	67.000	111.00	50.87	77.00	-120.00	44	475
Run 16	30.000	102.00	50.87	38.00	120.00	72	788
Run 17	20.000	56.00	50.87	77.00	-120.00	36	384
Run 18	13.000	85.00	50.87	-99.00	-180.00	72	782
Run 19	9.000	88.00	50.87	-125.0	-30.00	79	874
Run 20	18.000	130.00	50.87	77.00	-60.00	112	1233
Run 21	77.000	126.00	50.87	125.00	90.000	49	529

Table 5.2: Runs measured for Mn_4FeSi_3 using the Supernova.

5.1.4 Data reduction and corrections

After the search for reflections has been finished, the electronic measurements have to be transformed to usable diffraction intensities in a process called *data reduction*.

The goal of the data reduction is to obtain the magnitudes of the structure factors of each diffraction spot, via the square root of their measured intensities.

Data reduction procedure

In the CrysAlis^{Pro} data reduction software initially all spots above a certain intensity limit are searched. Using the algorithms incorporated in the software the orientation matrix is then determined. The UB or "orientation matrix" of the crystal relates the crystal coordinate system to the instrumental coordinate system[Busing, 1967]. Thus it contains the basic data for the definition of the reciprocal unit cell and its orientation in space. Once it is known, the position of each reciprocal lattice point may readily be calculated. The definition of the orientation matrix does vary to some extent from one instrument to another, mainly due to the fact that the reference systems are differently defined for different diffractometers.

Once the orientation matrix has been found the program can calculate the positions of reflections hkl and can then approximate the actual peak shapes with integration masks. As the outcome of the integration a list of hkl values with integrated intensities and standard deviations is produced.

For the measurement on Mn_4FeSi_3 the UB-matrix was fitted on the basis of 1056 peak positions. Altogether 2146 reflections were measured. On the basis of the peak positions and the measured intensities, the unit cell, the point group and the extinction rules can be determined. Mn_4FeSi_3 crystallizes in a primitive hexagonal lattice with unit cell parameters as shown in table 5.3:

a(Å)	b (Å)	c (Å)	V (Å ³)	Alpha	Beta	Gamma
6.8834(2)	6.8834(2)	4.7842(2)	196.3(1)	90°	90°	120°

Table 5.3: The unit cell parameters at ambient pressure

Numerical absorption correction

Numerical integration methods using the approximation with a Gaussian grid provide the best way to perform an absorption correction[Coppens,1970]. These methods require that the shape of the crystal is accurately described. To do so, the indices hkl of the faces need

to be determined and their distances from the center of the crystal have to be measured (Figure 5.6). Once this information is provided the path length for the incident and diffracted beam can be calculated and the corresponding transmission factors can be determined.

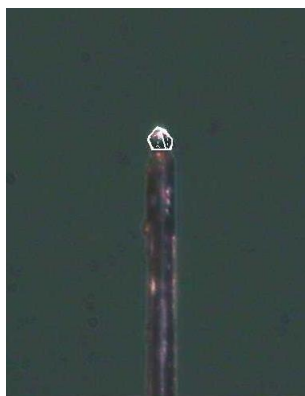


Figure 5.6: The single crystal of Mn_4FeSi_3 with the limiting faces

The correctness of the absorption correction is reflected by a reduction of the internal R-value $R(int)$ from 9.20% to 9.04%.

5.1.5 Structure determination

The program used in this study for structure refinement was Jana2006 [jana2006, 2010]. This is a versatile program and can be used to refine regular, modulated and composite crystal structures against single crystal or powder data collected with X-ray or neutron diffractometers. The structure determination process consists of several steps which will be described in the following.

Determination of the space group

First the data from the measurement on the Supernova which contains for each reflection hkl the integrated intensity and its standard deviation are imported into Jana2006. At the same time, the experimental parameters concerning the measurement and the lattice parameter are being imported. Once the data have been imported, the correct space group has to be determined. This is done in Jana2006 using an interactive wizard. The first step here is to determine the correct point group symmetry. For this, the data are averaged using all possible symmetries which are in accordance with the observed metrics (Table 5.4.) and the internal R-value is calculated.

The internal R-value is a measure for the internal consistency of the data set. It is calculated for observed reflections, where the measured intensity is larger than 3 times the

standard deviation ($I > 3\sigma I$) and for all the measured reflections separately. In the column “averaged” is the number of symmetry independent reflections after averaging and the redundancy provides the information about how many reflections have been averaged to give one symmetry independent reflection. As can be seen from the table the averaging of the data with point group symmetry 6/mmm gives the highest internal R-value. However, taking into account that the redundancy is significantly larger for this high symmetry, the probability that this is the correct point group symmetry is very high and it was therefore selected.

Crystal system	Point group symmetry	Rint(obs/all)	Averaged (obs/all)	Redundancy
Triclinic	-1	7.00/8.93	1901/3319	3.778
Monoclinic	2/m	7.89/9.66	1181/1793	6.993
Trigonal	-3	8.42/10.10	762/1117	11.225
Trigonal	-31m	8.79/10.30	446/615	20.387
Trigonal	3m1	8.81/10.32	439/652	19.23
Hexagonal	6/m	8.79/10.32	438/606	20.69
Hexagonal	6/mmm	9.04/10.42	271/337	33.257

Table 5.4: Test for the different Laue symmetries performed in Jana2006.

In the next step the data are analyzed with respect to observed extinction rules (Table 5.5). All the possible extinction rules for the hexagonal system are tested. The second column of Table 5.5 shows number of observed reflection over the total.

Space group	observed/Total	Ave(I/sig(I))
P6 ₃ /mcm	1/1086	3.096/0.407
P-6c2	1/1086	3.096/0.407
P6 ₃ cm	1/1086	3.096/0.407
P6 ₃ 22	0/19	0.000/0.459
P6/mmm	0/0	0.000/0.000

Table 5.5: Analysis of the extinction rules of different hexagonal space groups taken from Jana2006.

Formula	Mn ₄ FeSi ₃
Crystal system:	Hexagonal
Bravais-type:	P
Laue-symmetry:	6/mmm
Space group:	P6 ₃ /mcm
Number of formula units in the unit cell (Z):	2

Table 5.6: Structural details for Mn₄FeSi₃

{1} x y z	{13} -x -y -z
{2} -y x-y z	{14} y -x+y -z
{3} -x+y -x z	{15} x-y x -z
{4} -x -y z+1/2	{16} x y -z+1/2
{5} y -x+y z+1/2	{17} -y x-y -z+1/2
{6} x-y x z+1/2	{18} -x+y -x -z+1/2
{7} y x -z+1/2	{19} -y -x z+1/2
{8} x-y -y -z+1/2	{20} -x+y y z+1/2
{9} -x -x+y -z+1/2	{21} x x-y z+1/2
{10} -y -x -z	{22} y x z
{11} -x+y y -z	{23} x-y -y z
{12} x x-y -z	{24} -x -x+y z

Table 5.7: Symmetry operators of space group $P6_3/mcm$:

The column “obs/all” shows for each space group the number of reflections which should be systematically extinct. As can be seen from the table the extinction rule for the c-glide plane is nearly perfectly fulfilled.

For the space groups with the c-glide plane “obs/all” = 1/1086, which means that the total number of measured reflections sensitive to the corresponding extinction rule is 1086 and only one of them violates the rule as it has an intensity which is higher than 3 times the error. On the basis of the above described analysis, we chose the centrosymmetric space group $P6_3/mcm$ for the structure refinement (Table 5.6). This is in accordance with the space group suggested in earlier investigations [Binczyska et al, 1973; Johnson, 1972]. The symmetry operators for this space group are given in Table 5.7.

Structure solution

Jana2006 does not contain the necessary algorithms for structure solution and calls external programs instead. The program used in this study is Superflip which uses the charge flipping algorithm [Jana2006, 2006].

Superflip provides an additional test on the space group symmetry, as it solves the structure with the minimum symmetry P1 and then searches for symmetry elements in the obtained solution. The space group suggested from the symmetry search in Superflip is $P6_3/mcm$ and thus the same as the one obtained earlier. The initial structural model found by Superflip is saved to the file *m40-file*.

Structure refinement

In this step the structural model found by Superflip is further refined as the initial atomic coordinates obtained from the structure solution are not very precise and the description of the displacement parameters has to be improved. The refinement is a least-square process where individual parameters (scale factor, atomic coordinates, occupation factors, displacement factors) are varied to obtain the best agreement between observed and calculated structure factors. The quality of the refinement is expressed by various residuals, the most important one being the conventional R-value. The **R-value** is a measure for the quality of a structure refinement and indicates the agreement between the calculated structural model and the experimentally measured X-ray diffraction intensities. It is defined as

$$R(int) = \frac{\sum_{hkl} ||F_o| - |F_c||}{\sum_{hkl} |F_o|} \quad 5.1$$

Where F_o is the observed structure factor and F_c is the calculated structure factor. A weighted R-factor (wR) is often used, where an additional weighting based on the standard deviation of the observed structure factors is taken into account [Jones, 1979].

$$wR = \frac{\sum_{hkl} w^{1/2} |F_o - F_c|}{\sum_{hkl} w^{1/2} F_o} \quad 5.2$$

Refinement of the mixed occupancy sites

According to the structure solution and the subsequent refinement up to this stage, there are three symmetry independent sites in the unit cell (Table 5.8). This stage of the refinement corresponded to a model where the M1- site is completely occupied by Fe, while the M2-site is fully occupied by Mn

Atoms	occupancy parameters (ai)	x	Y	Z
M1 (Fe)	0.166667(4)	0.66667(4)	0.33333(5)	0.0(3)
M2 (Mn)	0.25(8)	0.76639(5)	1.00(9)	0.25(3)
Si1	0.25(6)	0.59822(6)	0.59822(8)	0.25(3)

Table 5.8: Occupancy parameters(ai) for the atoms before the refinement of the mixed occupancy site.

However, these occupancies lead to an incorrect formula of $Mn_3Fe_2Si_3$. The scattering factor curves for Mn and Fe are very similar in x-ray diffraction due to the fact that they possess similar number of electrons and it is very difficult to distinguish them. However, from neutron powder diffraction data, where Mn and Fe are easily distinguishable, it is known that the M1 site is occupied partially by Fe and Mn while the M2 site is fully

occupied by Mn [Hering et al, 2014]. The mixed occupancy was introduced into Jana2006 in the following way: Two atoms Fe1 and Mn1 were put onto the M1 site. Their coordinates and displacement parameters were restricted to be equal and the occupancy factors were set to 0.0833(6) for both atoms resulting in the correct stoichiometry Mn_4FeSi_3 (Table 5.9).

Atoms	occupancy parameters (ai)	x	Y	Z
Fe1	0.0833(6)	0.66667(6)	0.33333(5)	0.0(3)
Mn1	0.0833(6)	0.66667(6)	0.33333(5)	0.0(3)
Mn2	0.25(8)	0.76639(5)	1.00(9)	0.25(3)
Si1	0.25(6)	0.59822(6)	0.59822(8)	0.25(3)

Table 5.99: Atomic coordinates and occupancy parameters in the final refinement.

Refinement of atomic displacement parameters

In the last step of the refinement the atomic displacement parameters (ADPs), which describe the small thermal displacements of the atoms, are refined. They are a measure of the extent to which the atoms move around their equilibrium position.

Atoms	U11	U22	U33	U12	U13	U23
Fe1	0.006544(0)	0.006544(0)	0.004692(0)	0.003272(0)	0	0
Mn1	0.006544(13)	0.006544(0)	0.004692(16)	0.003272(0)	0	0
Mn2	0.00778(13)	0.005515(16)	0.00885(15)	0.002757	0	0
Si1	0.005991(2)	0.005991(2)	0.007972(2)	0.003408(2)	0	0

Table 5.10: Anisotropic displacement parameters [\AA^2] for Mn_4FeSi_3

As in solids atoms normally do not move in an isotropic way but mostly in favored directions, it is necessary to describe the displacement by anisotropic “harmonic” displacement ellipsoids. Six parameters are used to describe anisotropic thermal motion.

$x[Fe1]=0.66667$	$y[Mn2]=1$	$y[Si1]=x[Si1]$
$y[Fe1]=0.33333$	$z[Mn2]=0.25$	$z[Si1]=0.25$
$z[Fe1]=0$	$U12[Mn2]=0.5*U22[Mn2]$	$U22[Si1]=U11[Si1]$
$U22[Fe1]=U11[Fe1]$	$U13[Mn2]=0$	$U13[Si1]=0$
$U12[Fe1]=0.5*U11[Fe1]$	$U23[Mn2]=0$	$U23[Si1]=0$
$U13[Fe1]=0$		
$U23[Fe1]=0$		

Table 5.11: Equations induced by symmetry

These are the displacements along the three main axes of the ellipsoid, called U11, U22 and U33, as well as the three mixed parameters U12, U13 and U23 containing the orientations of the three main axes of the ellipsoids towards the crystallographic axes. The

results for Mn_4FeSi_3 are shown in Table 5.10. Equations induced by the symmetry that lead to restrictions on certain atomic parameters in special positions are given in Table 5.11.

5.2 Single Crystal Structure Determination at High Pressure

The procedure used for the structure determination from single crystal data under high pressure is in principle the same as in the previous section. Yet, in this case data were measured with the crystal enclosed in a diamond anvil cell and a STOEIPDS diffractometer was used. The X-Area software was used for data reduction [X-Area, 2006] and the program Absorb GUI was employed for the absorption correction [Angel, 2013]. The compound Mn_4FeSi_3 was measured at six different pressure points.

5.2.1 Loading the sample to the diamond anvil cell

A suitable crystal was selected using the criteria described earlier. For the high pressure experiments the sample was initially loaded into a diamond anvil cell equipped with diamonds with a culet of $500\mu\text{m}$ along with two small chips of ruby under the microscope. The sample has to be very small to fit into the distance between the diamond culets to avoid crushing the sample when closing the diamond anvil cell and when increasing the pressure. The ruby chips were small when compared to the sample to keep the diffraction intensities from ruby as low as possible. The sample was then immersed into the pressure transmitting medium (a mixture of 4:1 methanol/ethanol) which was loaded into the gasket hole. Care was taken in order to avoid flushing out either the sample or the ruby during the flooding of the sample chamber with the pressure-transmitting medium. Finally the diamond anvil cell was closed and, if the procedure was successful, the pressure can now be built up.

Pressure measurements

The sample was measured at six different pressure points (Table 5.12). The pressure was deduced by measuring the shift of the lines in the luminescence spectra of ruby, as explained previously (section 4.3.2).

5.2.2 Data collection

For the high pressure measurements a STOEIPDS (Imaging Plate Diffraction System) 2-circle diffractometer was used for recording the diffraction intensities. The diamond anvil cell was mounted on a standard goniometer head and fixed to the ϕ -circle of the diffractometer. A picture of the experimental setup is shown in (Figure 5.7). The data

collection parameters for all six pressure points are given in (Table 5.12). The sample was optically centered to make it coincide with the crosshairs of the built-in video camera. An ω -scan in the range from 0-180° was used for data collection. (Table 5.13) gives an overview over the measured run list.

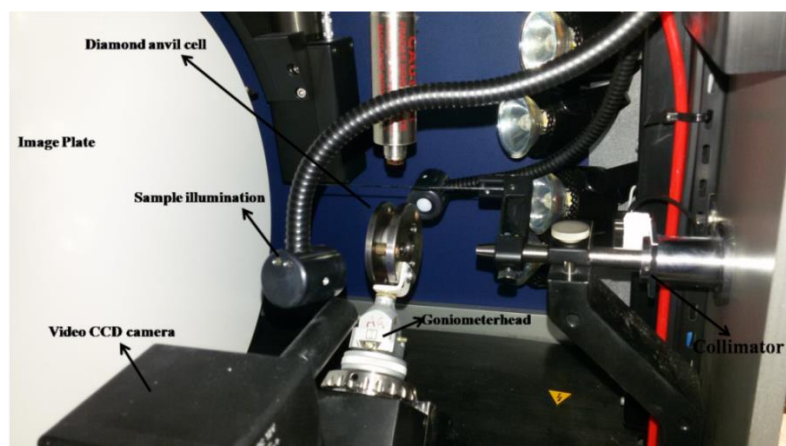


Figure 5.7: STOEIPDS (Imaging Plate Diffraction System) diffractometer with the mounted diamond anvil cell at the Institute for Crystallography at the Rheinisch-Westfälisch-Technische University in Aachen.

Wavelength [\AA]	0.71073
Tube power [kW]	1.25
Tube voltage [kV]	50
Tube current [mA]	25
Collimator size [mm]	0.5
Temperature [K]	298
Detector distance [mm]	180
2theta range	1.27 - 43.36
d(hkl) range [\AA]	31.989 - 0.962

Table 5.12: Instrumental parameters for the data collection

Pressure point (GPa)	# of Run	ω range	Φ	# of frames	Independent reflection
0.425	18	0-180	0-350	326	4150
0.9	18	0-180	0-350	310	3985
2.105	18	0-180	0-350	310	4665
3.145	18	0-180	0-350	310	3191
4.8	14	0-180	0-350	253	2837
6.21	14	0-180	0-350	253	2755

Table 5.13: Summary of the run list used for the data collection for Mn_4FeSi_3 at all pressure points

5.2.3 Data reduction and corrections

Due to the use of a diamond anvil cell for the high pressure experiments, additional problems occur in the data collection and subsequent treatment of the data. There is a number of possible interactions between the cell components and the X-ray beams, e.g. interaction with the diamond anvils and the gasket. A representative frame illustrating this is shown in (Figure 5.8).

The scattering of the X-rays by the diamond anvils gives rise to extremely strong diffracted beams with high intensity which are recorded on the detector. Reflections affected by overlap with the diamond anvil reflections can be rejected during the integration. When the cell is rotated around ω and φ both the incident and the scattered beams can hit the body of the diamond anvil cells which can cause shadowed regions on the measured frames if the opening angle of the diamond anvil cell is exceeded. This problem can be taken care of by the application of masks on the shaded regions when integrating the intensities.

Peak search

The first step after the collection of the data is the peak search. The X-Area program performs the peak search over a series of images and stores the information on the peak positions in the parameter file. In the initial search process some diamond peaks and peaks lying on the powder rings from the gasket are included along with the sample peaks, but they are easy to identify later on.

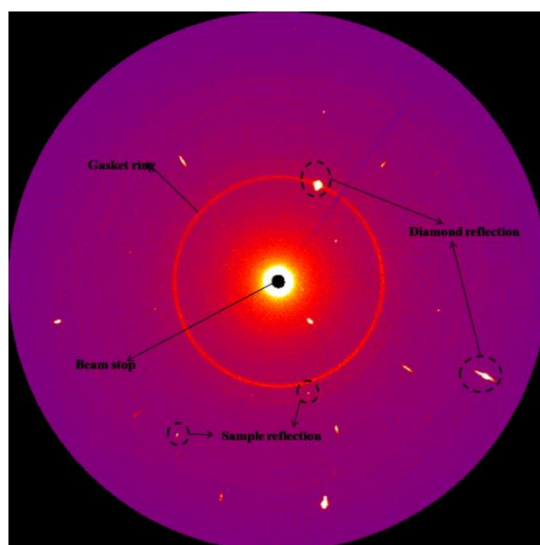


Figure 5.8: Representative frame for the high pressure measurements: Diamond reflection, sample reflection and gasket ring are indicated.

Indexing

(Figure 5.9a) illustrates the indexing process incorporated into X-Area [X-Area, 2006]. All peak positions are projected onto the horizontal plan of the Ewald sphere, resulting in a series of sharp “lines”. Each “line” represents a direction in the reciprocal space [X-Area, 2006]. The most intense peaks result from the diamond reflections. They can be selected and used to obtain the orientation matrices of the diamonds.

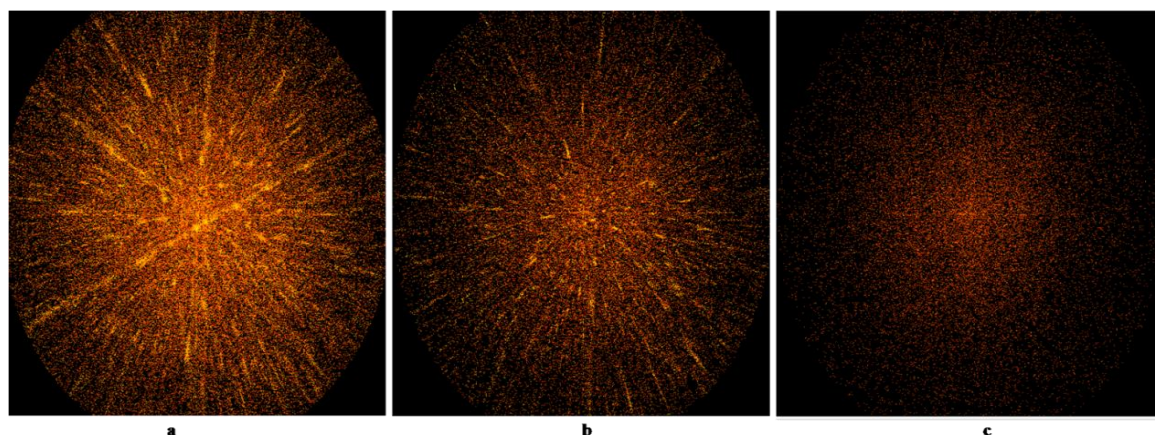


Figure 5.9: (a) Original picture including all found peaks. The brightest lines represent diamond reflections. (b) Picture dominated by reflections from the sample after deleting the diamond reflection. (c) Peaks resulting from the gasket after deleting diamond and sample reflections.

Once the orientation matrices for the diamonds have been found all peaks indexed with the matrices can be deleted. After this the resulting picture is dominated by the sample reflections (Figure 5.9b). Now the lattice parameter and the orientation matrix for the sample can be determined. If these reflections are also deleted, a picture like in (Figure 5.8c) remains in which there are only the reflections from the polycrystalline gasket left over. Care was taken that the crystal axis were oriented the same way in the measurements at the different pressures to ensure that all the integrated intensities were directly comparable.

Integration Once the orientation matrix is known, the software can calculate the individual reflection positions on all the frames. In the integration procedure each frame is sequentially scanned and at each calculated reflection position (hkl) an integration mask is superimposed to produce a dataset consisting of indices (hkl) and their integrated intensity with an estimate of their intensities $I(hkl)$ and the standard uncertainties of the intensities $\sigma(I)$. The individual steps followed in the integration routine by the program X-Area are the following:

Optimization: Determination of the optimal parameters for A, B and EMS.

Peak and background during the integration are defined with the coefficient A and B , which describe elliptical masks in the program [X-Area, 2006]. The parameter EMS is the Effective Mosaic Spread and results from the divergence of the primary beam and the mosaic spread of a crystal. Its value is optimized by evaluating different trial integrations performed by the program [X-Area, 2006]. Values of A, B and EMS parameters used for the integration of the data at all pressure points were 25, 10, and 0.023 respectively (Figure 5.10).

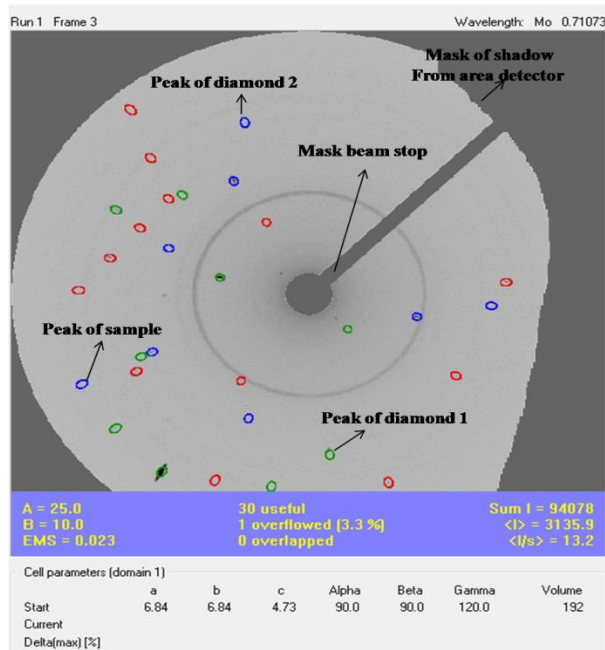


Figure 5.10: Representative frame of the high pressure measurements on Mn_4FeSi_3 . The integration masks are indicated and the masks for the beam stop and the shadowed area of the detector are visible.

During the integration the region of the frame which are shadowed by the beam stop and the diamond anvil cell are masked and are then skipped in the integration (see Figure 5.10). At the end of the integration a post-refinement of the lattice parameter and orientation matrix based on the positions of the integrated reflections is carried out.

Absorption Correction

The absorption correction at high pressure is more complex than at ambient pressure as, in addition to absorption by the crystal, the X-ray beam also suffers absorption by the diamond anvils through which they pass. The absorption correction for the diamonds was performed with the program ABSORB7 GUI [Angel, 2013] for all pressure points.

5.2.4 Data refinement and structure solution

In principle, the structure refinement of diffraction data at high pressures is similar to the one performed at ambient pressure (*see section 5.1.2-5.1.5*). However, although the effect

of the different components of the DAC on the diffracted intensities has already been partially reduced in the steps described earlier, there still remain some “outliers“ in the reflection data which have falsified intensities. During the refinement these reflections have to be identified and rejected with the algorithm implemented into Jana2006. The procedures are described in detail [Friese, 2013].

Identification and rejection of outliers

There are a number of ways to identify outliers[Friese, 2013], the most important one being the comparison of symmetry-equivalent reflections. Individual reflections with intensities showing large deviations from the average intensity value for a group of symmetry equivalent reflections can be easily identified using the graphical interface in Jana2006 and can then be rejected in the interactive manual culling dialogue (Figures 5.11 and 5.12).

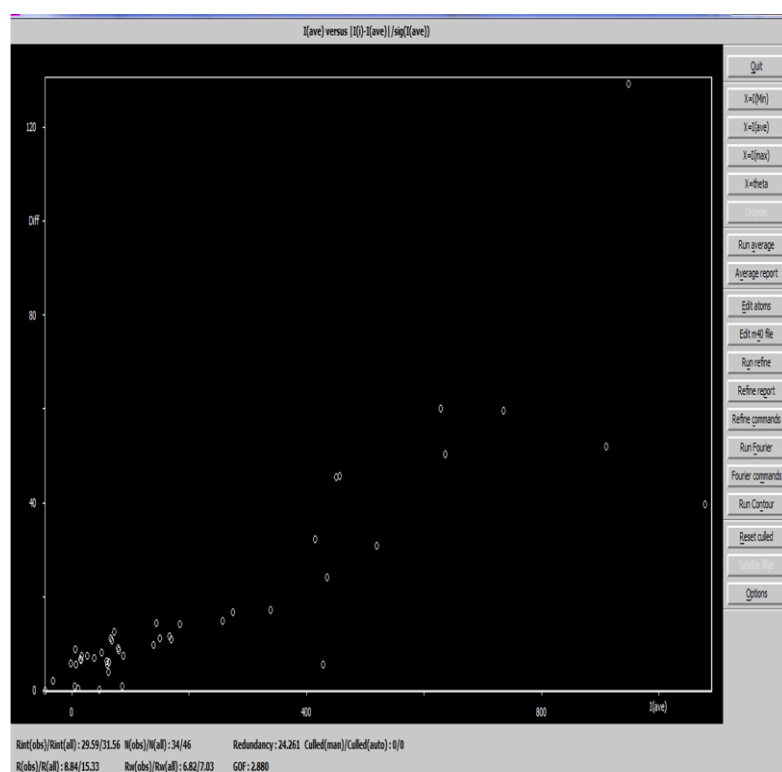


Figure 5.11: Screenshot of the graphical interface in the manual culling menu of Jana2006. The x parameter can be changed between four different values (I(min), I(max), I(average) and θ). The y-parameter represents the intensity of the individual reflections I(i) compared with the average intensity I(average) using the value $\Delta = |I(i) - I(\text{average})| / \sigma I(\text{average})$ [Friese, 2013].

In the example in (Figure 5.12), the first weak reflection in the group has too small an intensity due to the falsification caused by overlay with the powder ring from the gasket which leads to an increased background. In other cases, reflection intensities can be too high due to superposition with tails of the very strong diamond reflections. The exclusion

of “outliers” leads to a decrease in the internal R-value. For example, the R(int) for the dataset at 0.425 GPa without applying any culling is $R_{\text{int}}(\text{obs})/R_{\text{int}}(\text{all}):29.59/31.56$, after careful rejection of 38 outliers it is $R_{\text{int}}(\text{obs})/R_{\text{int}}(\text{all}):11.98/14.27$.

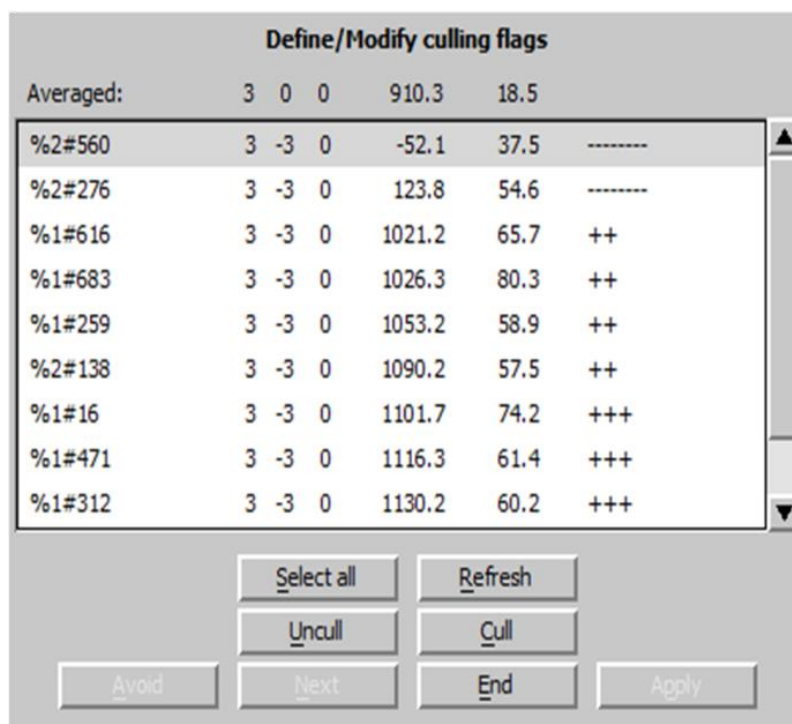


Figure 5.12. Detail of the graphical interface in the manual culling menu of Jana2006.

Once most of the outliers are rejected, the structure refinement can proceed in a similar way to the one described for the ambient data. (Table 5.14) provides an overview over the results of the structure refinement at the different pressure points.

Crystal data	(I) 0.0001GPa	(II) 0.425GPa	(III) 0.9GPa	(IV) 2.105GPa
Chemical formula	Mn ₄ FeSi ₃			
Crystal system, space group	Hexagonal, P6 ₃ /mcm	Hexagonal, P6 ₃ /mcm	Hexagonal, P6 ₃ /mcm	Hexagonal, P6 ₃ /mcm
No. of measured reflections (obs/all)	5681/11452	322/1028	314/987	524/1123
No. of independent reflections (obs/all)	271/329	34/45	33/44	35/44
R(int) (obs/all)	9.04/10.04	11.98/14.27	13.66/16.07	9.48/10.67
R(obs)/R(all)	1.82/2.99	3.97/8.39	4.17/621	3.06/5.47
R(w)(obs)/R(w)(all)	2.00/2.32	4.88/5.02	4.68/4.83	4.07/4.14

No. Of culled reflections	0	38	7	16
Crystal data	(V) 3.145GPa	(VI) 4.8GPa	(VII) 6.21Gpa	
Chemical formula	Mn₄FeSi₃	Mn₄FeSi₃	Mn₄FeSi₃	
Crystal system, space group	Hexagonal, P63/mcm	Hexagonal, P63/mcm	Hexagonal,P63/mcm	
No. of measured reflections (obs/all)	344/1125	221/819	191/812	
No. of independent reflections (obs/all)	35/44	30/45	28/44	
R(int) (obs/all)	11.43/13.38	12.85/15.71	18.16/23.61	
R(obs)/R(all)	4.64/6.59	4.34/8.02	4.96/8.55	
R(w)(obs)/R(w)(all)	5.47/5.51	4.75/4.89	5.86/6.11	
No.of culled reflections	38	46	73	

Table 5.14: Details on the structure refinement of Mn₄FeSi₃ at the different pressure points.

Chapter 6 Powder Diffraction

Powder and single-crystal X-ray diffraction are the two main methods in the field of crystal structure determination of materials. In this study both powder and single X-ray crystal diffraction experiments have been carried out on Mn_4FeSi_3 . The results from the two methods complement each other very well. Single crystal diffraction was used to determine the symmetry, atomic coordinates, and atomic displacement parameters (ADPs). In addition, powder diffraction at a synchrotron beamline was used to determine precise lattice parameter as a function of pressure. This chapter gives a short introduction to high pressure X-Ray powder diffraction and then provides details on the experiments carried out at beamline ID09a of the European Synchrotron Radiation Facility (ESRF) in Grenoble, France.

6.1 High Pressure X-Ray Powder Diffraction

Synchrotron radiation of high brilliance was used for in situ high-pressure powder diffraction experiments. The quality of the high pressure powder diffraction data from synchrotron sources is such that reliable unit-cell parameters can be obtained and even structural parameters can be extracted for simple systems. A sketch of a high pressure powder diffraction experiment is shown in (Figure 6.1).

The experiments have been carried out on beamline ID09A of the European Synchrotron Radiation Facility (ESRF) in Grenoble, France, at a wavelength of $\lambda = 0.41038 \text{ \AA}$ (Figure 6.2). The beamline is dedicated to the determination of structural properties of solids at high pressure. A spherical mirror and a bent Silicon (111) monochromatic focus the white beam from the insertion device. The typical beam size at the sample is $30 \times 30 \text{ \mu m}^2$ but can even be decreased to sizes as small as $10 \times 10 \text{ \mu m}^2$ for mega bar pressure experiments.

A 2-dimensional Mar555 image-plate detector is used for recording of the diffraction data. The use of a 2-dimensional detector is advantageous as the entire diffraction cone can be collected and therefore effects due to, e.g. sample texture can be identified before the integration of the 2-dimensional data into the conventional 1-dimensional intensity vs. 2θ data-set, which is used for refinement. The possibility to read-out the data from image plates in situ allows to collect powder diffraction data of sufficient quality within exposure times below 1 minute [Bauchau et al, 1998].

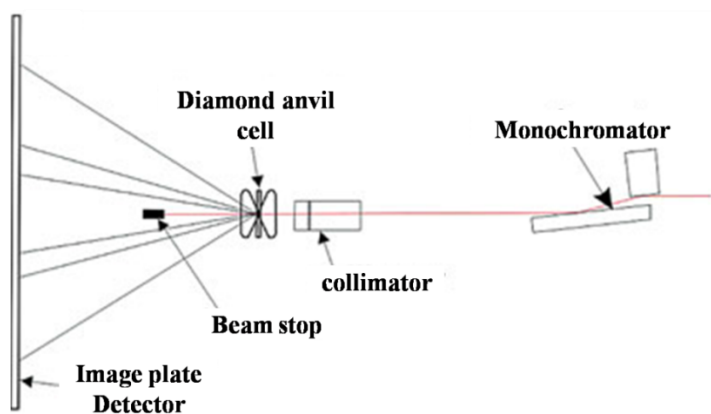


Figure 6.1: Illustration of the key components of a high-pressure X-ray powder diffraction experiment.

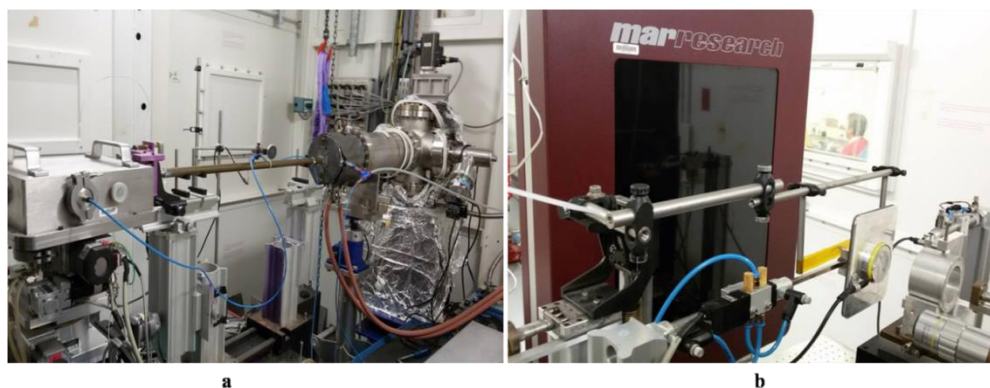


Figure 6.2: a. Beamline ID09A at the European Synchrotron Radiation Facility ESRF, b. The image plate detector Mar555.

The experiments have been carried out using a membrane-type diamond anvil cell [Letoullec,1998]. In these cells the force is generated by inflating a metal membrane whose expansion pushes the diamond anvils.

6.2 Processing of the Powder Diffraction Data

Over 55 pressure points were measured at constant temperature 298 K for Mn_4FeSi_3 . The 2-dimensional patterns were integrated to provide the one-dimensional powder diffraction pattern using the program Fit2D [Hammersley,1996]. The obtained patterns were refined with the LeBail method [Lebail,1988], using the program Jana2006 [Jana2006, see also Figure 6.3]. From the LeBail refinement lattice parameter and unit cell volumes can be extracted.

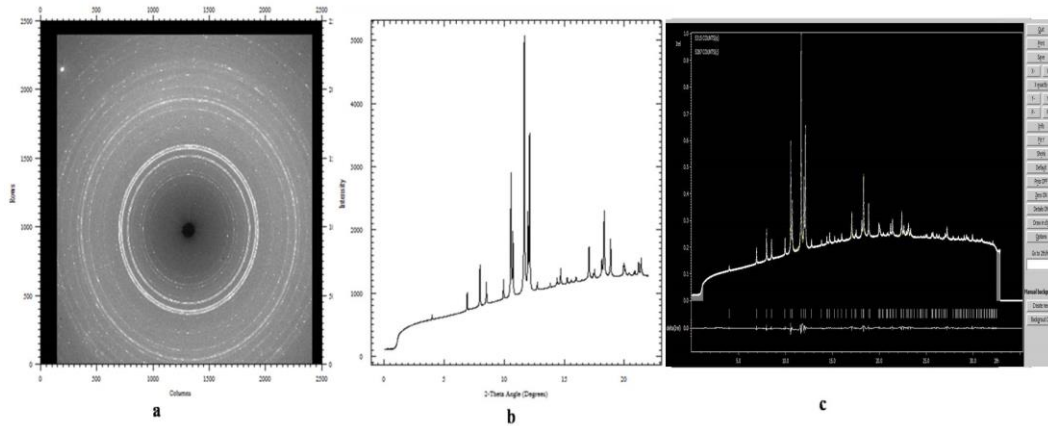


Figure 6.3. Stages of data processing of the powder diffraction data. The raw image collected on the Mar555 detector is shown in part (a). The concentric rings correspond to the diffracted intensities from the sample; the bright spot at the upper left corner of the image is an intense diamond reflection from the DAC. These spots have to be masked to avoid contamination of the sample diffraction pattern. Part (b) shows the 1-dimensional pattern obtained by integration with the programme FIT2D. The elevated background is due to scattering from the components of the DAC. Part (c) Screenshot of the LeBail-refinement of the data carried out with Jana2006.

6.3 Equation of State “EOS”

An equation of state is a thermodynamic equation describing the connection between various macroscopically measurable properties of a system. Most EOS are written to express functional relationships between P, T and V. There are many semi-empirical relations in use to describe the pressure-volume behavior of solids in terms of at most three parameters. For this study the most relevant formulations are the Murnaghan relation [Murnaghan, 1944]. The Murnaghan equation of state is based on the laws of elasticity and the assumption that the bulk modulus is proportional to pressure [Thibault, 2009]. The pressure may then be expressed as.

$$P(V) = \frac{B_0}{B'} \left[\left(\frac{V}{V_0} \right)^{-B'} - 1 \right] \quad 6.1$$

Further details about the methods of data analysis and assessment of the results are provided in the next chapter. In this study the program EosFit7 GUI [Angel, 2014] was used for the fitting of a P-V dataset.

Chapter 7 Results and discussion

In this chapter the analysis and the results of the powder and single crystal investigations is presented. Initially, the crystal structure at ambient conditions is described and then compared to previous studies. Then the effect of pressure on the lattice parameter and unit cell volume is described. Finally, the pressure-induced changes in the interatomic distance are discussed.

7.1 Crystal Structure of Mn_4FeSi_3 at Ambient Conditions

According to the results of the refinement of the single crystal diffraction data described in Chapter 5 the compound Mn_4FeSi_3 crystallizes in the hexagonal space group $P6_3/mcm$ at ambient and high pressures. The lattice parameter and atomic coordinates at ambient conditions are comparable to the earlier results from the literature [Binczyska et al. **AI**].

Within the unit cell three symmetrically independent positions are occupied. The 4d Wyckoff position (site symmetry $32; 2/3, 1/3, 0$) shows mixed occupancy of Fe1 and Mn1, the 6g position (site symmetry $mm; x, 0, 1/4$) is exclusively occupied by manganese (Mn2) and a second 6g position ($x', 0, 1/4$) is occupied by the Si atoms. If one disregards the atomic displacement parameters, only the x -coordinate of Mn2 and Si1 are free atomic parameters.

The Mn1/Fe1 atoms are coordinated by six silicon atoms in the shape of an octahedron. Neighboring $[\text{Mn1/Fe1Si}_6]$ –octahedron share common faces and form chains parallel to the c -direction. The Mn2 atoms form octahedron with neighboring Mn2 atoms. The centers of these octahedra remain empty. A schematic view of the structure is shown in (Figure 7. 1) and (Figure 7.2).

The main difference to earlier data published in the literature concerns the distribution of Mn and Fe: according to Binczyska et al [Binczyska et al. **AI**] iron is mainly incorporated on Wyckoff position 4d ($2/3, 1/3, 0$) which is occupied by $0.577 \text{ Mn} + 0.423 \text{ Fe}$. The remaining iron is on Wyckoff position 6g (0.949 Mn and 0.051 Fe). In contrast to this, our model shows that all the iron is on WP 4d ($0.5\text{Fe1}+0.5\text{Mn1}$), while Wyckoff position 6g is exclusively occupied by Mn2 ($x, 0, 1/4$). This difference could be related to

different synthesis conditions, which induce a different degree of order of the magnetic ions.

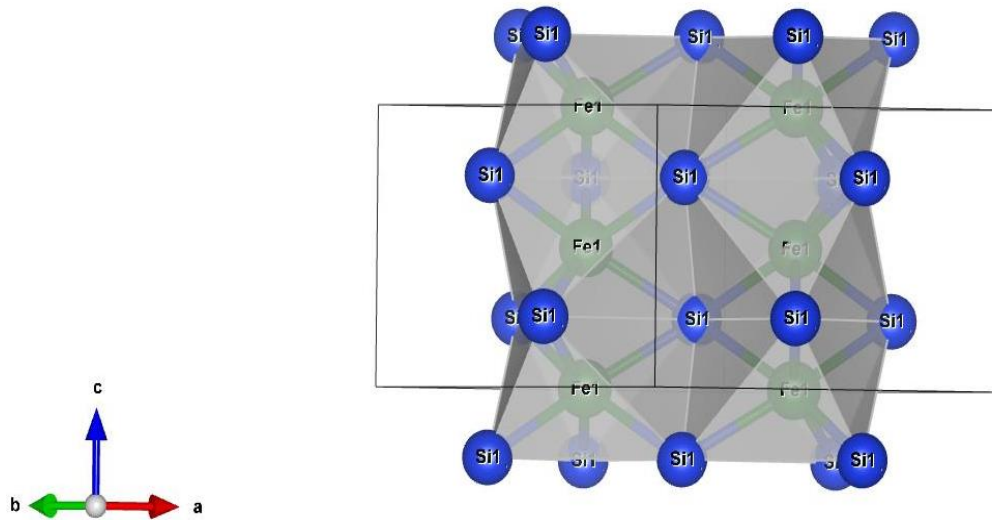


Figure7. 1: Schematic view of the structure of Mn_4FeSi_3 . Coordination polyhedra around Fe1\Mn1 are indicated.

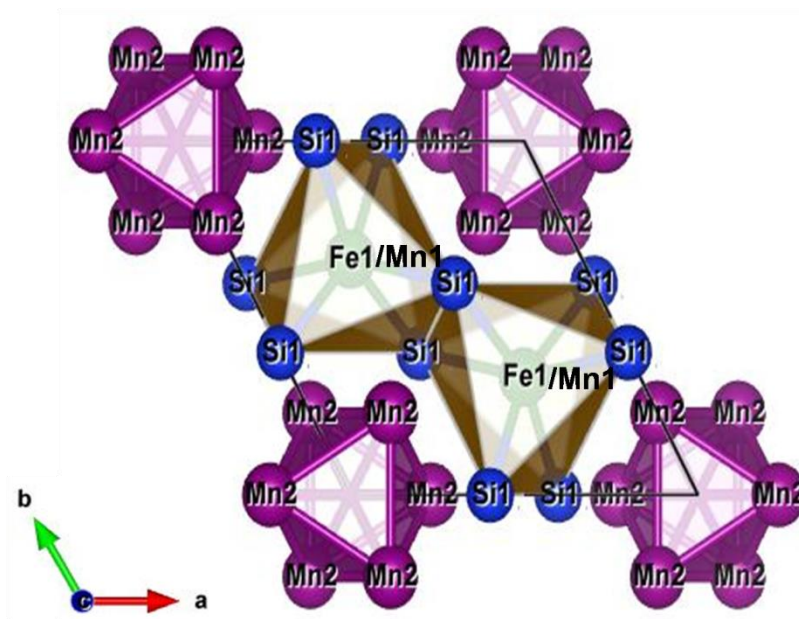


Figure7. 2: Schematic view of the structure of Mn_4FeSi_3 along the c-axis. Coordination polyhedra around Fe1\Mn1 and Mn2 are indicated.

7.2 Effect of Pressure on the Lattice Parameter and Unit Cell Volume

From the LeBail refinements of the high pressure data the pressure dependence of the lattice parameter and unit cell volumes were extracted (Table 7.1). The lattice parameters of Mn_4FeSi_3 as a function of pressure are portrayed in (Figure 7.3). With increasing pressure both lattice parameters a and c monotonously decrease.

Pressure (GPa)	a (Å)	c (Å)	v (Å ³)	Pressure (GPa)	a (Å)	c (Å)	v (Å ³)
0.1	6.88141(35)	4.78265(25)	196.135	1.97	6.84582(21)	4.75689(28)	193.07
0.1	6.88141(35)	4.78265(25)	196.135	2	6.84492(11)	4.75639(28)	192.994
0.1	6.88097(14)	4.78281(18)	196.111	2.05	6.84366(25)	4.75539(33)	192.882
0.16	6.88006(11)	4.78222(29)	196.04	2.12	6.84231(11)	4.75447(27)	192.769
0.2	6.87904(16)	4.78141(21)	195.953	2.18	6.84106(19)	4.75334(26)	192.653
0.27	6.87778(15)	4.78082(19)	195.853	2.24	6.8395(18)	4.75267(25)	192.538
0.36	6.87609(17)	4.77908(20)	195.685	2.29	6.83779(11)	4.75187(26)	192.401
0.425	6.8899(17)	4.778(20)	196.43	2.35	6.83675(11)	4.75071(26)	192.307
0.44	6.87435(20)	4.77766(26)	195.528	2.41	6.83589(18)	4.74979(25)	192.218
0.53	6.87235(15)	4.77693(19)	195.385	2.5	6.83428(20)	4.74855(27)	192.078
0.61	6.87037(17)	4.77564(20)	195.219	2.6	6.83262(11)	4.74685(27)	191.916
0.74	6.86792(15)	4.77373(19)	195.002	2.79	6.82913(21)	4.74474(29)	191.635
0.82	6.86646(14)	4.77286(18)	194.884	2.85	6.82829(19)	4.74416(27)	191.564
0.9	6.86608(21)	4.77231(27)	194.834	2.91	6.82703(18)	4.74268(24)	191.434
0.94	6.86511(19)	4.77139(26)	194.747	2.96	6.82545(18)	4.74222(24)	191.326
1.03	6.86291(21)	4.76986(29)	194.556	3.145	6.8329(20)	4.7278(20)	191.17
1.08	6.8611(20)	4.76887(28)	194.47	3.05	6.82348(16)	4.74108(22)	191.17
1.14	6.8607(20)	4.76856(28)	194.38	3.365	6.81771(19)	4.73662(26)	190.667
1.21	6.8594(20)	4.76764(27)	194.271	4.8	6.8073(20)	4.7196(20)	189.4
1.31	6.85711(17)	4.76622(23)	194.088	3.61	6.81361(11)	4.73374(27)	190.327
1.41	6.85609(18)	4.76433(26)	193.948	4.31	6.80163(21)	4.72511(29)	189.31
1.46	6.85452(18)	4.76367(26)	193.833	6.21	6.7894(20)	4.6935(20)	187.37
1.54	6.85329(17)	4.76312(25)	193.74	4.635	6.79659(22)	4.72179(31)	188.895
1.63	6.85155(19)	4.76128(26)	193.567	5.295	6.78651(17)	4.71376(24)	188.019
1.71	6.85013(22)	4.76008(30)	193.44	5.89	6.77693(16)	4.70696(23)	187.214
1.77	6.84937(11)	4.75976(26)	193.382	7.155	6.75591(18)	4.69266(25)	185.488
1.81	6.8489(20)	4.75913(28)	193.33	8.2	6.74099(20)	4.68084(28)	184.205
1.86	6.84774(20)	4.75829(28)	193.231	9.03	6.73016(11)	4.67265(28)	183.292
1.91	6.84685(20)	4.75761(28)	193.157	9.99	6.71709(16)	4.66283(23)	182.198
				10.92	6.70532(18)	4.65384(26)	181.201

Table 7.1 Lattice parameter and unit cell volumes for the different pressure points as extracted from the LeBail refinement.

As can be seen from the plot of the normalized lattice parameter (Figure 7.4), the relative change in the *a* and the *c* lattice parameter as a function of pressure is nearly identical indicating an almost isotropic compression.

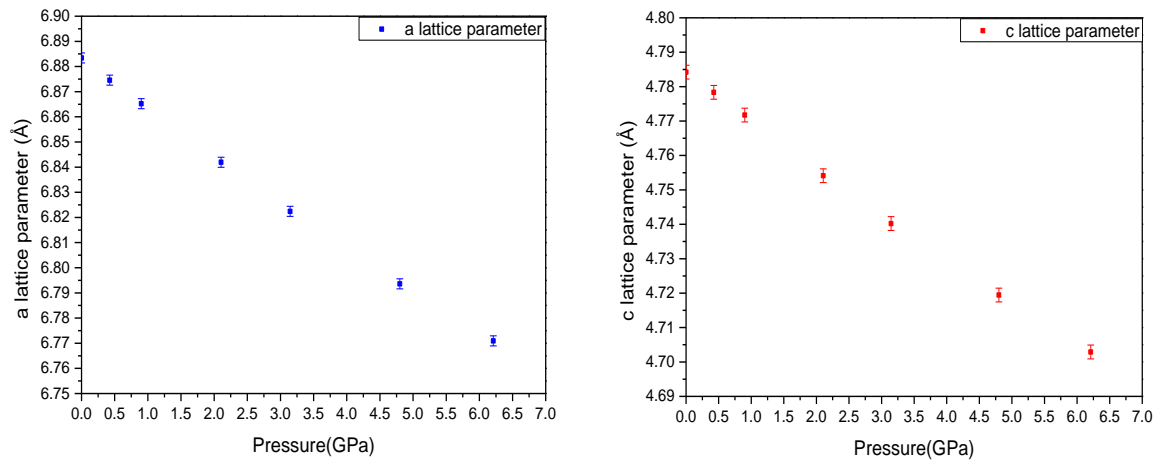


Figure 7.3: Pressure dependence of the lattice parameter of Mn_4FeSi_3 . The lattice parameters were extracted from LeBail fits of the powder diffraction measurements performed at ID09A of the ESRF.

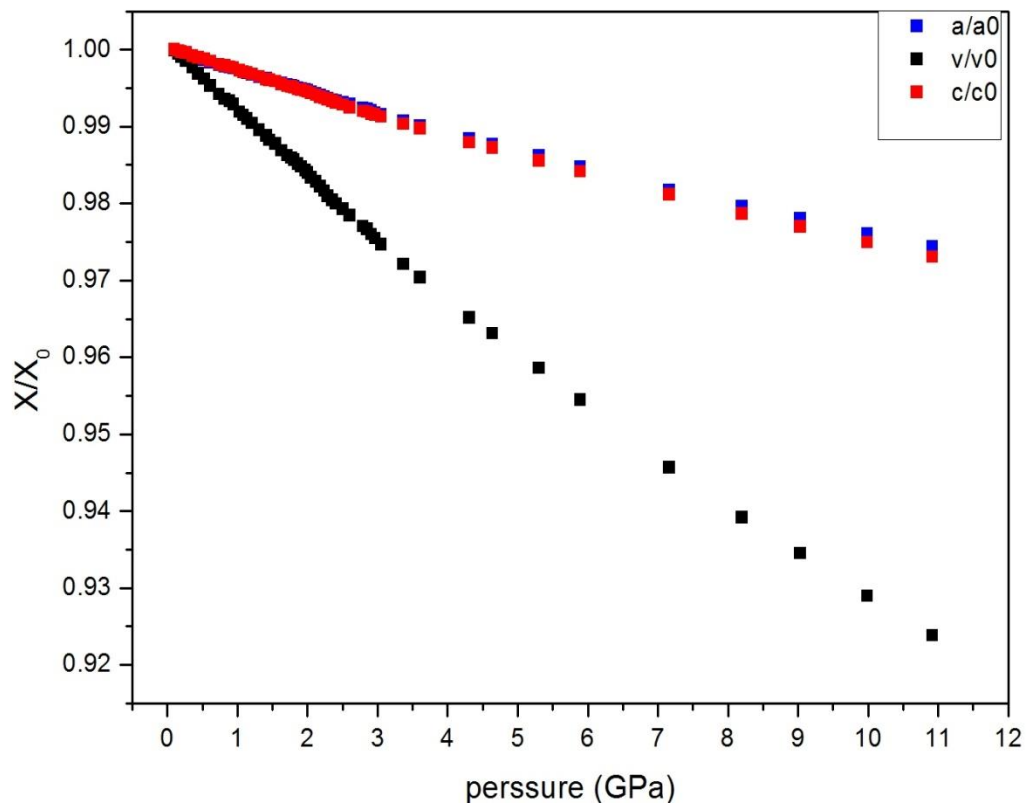


Figure 7.4: Pressure dependence of the normalized lattice parameters as extracted from the powder diffraction data measured at beamline ID09A

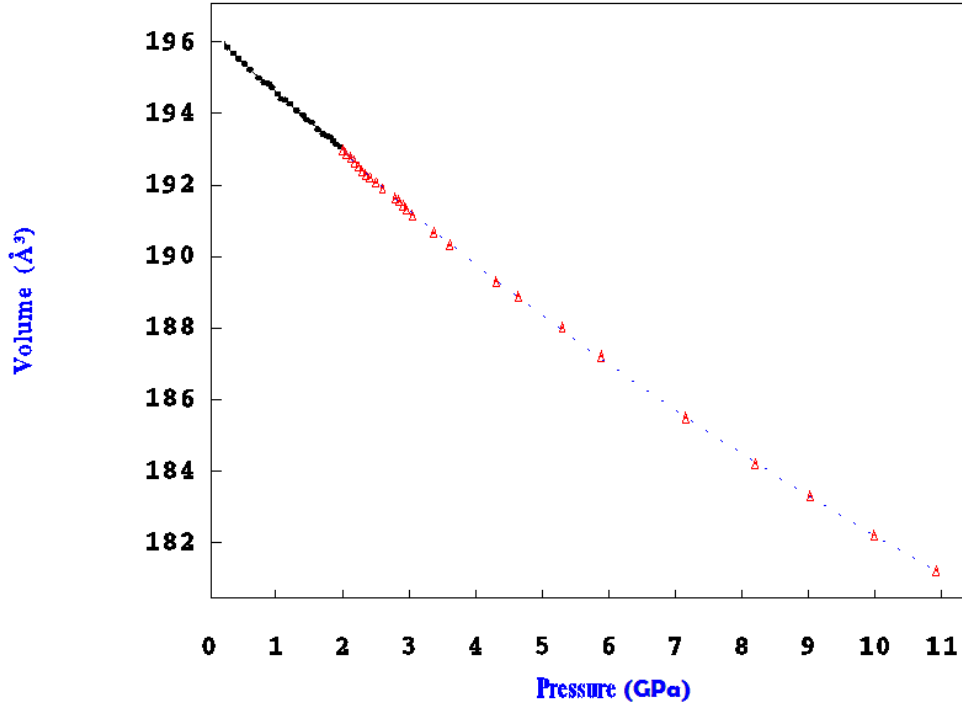


Figure 7.5: Pressure dependence of the unit-cell volume of Mn_4FeSi_3 . The data are based on synchrotron powder diffraction measurements at Beamline ID09a of the ESRF. Two equations of state were fitted to the data, one for the lower pressure range up to 2 GPa, a second one for the higher pressure range.

The variation of the unit cell volume with pressure is represented in (Figure 7.5). One observes a continuous decrease of the unit cell volume with increase in pressure. The data were fitted with a Murnaghan equation of state [Murnaghan,1944].

$$P(V) = \frac{B_0}{B'} \left[\left(\frac{V}{V_0} \right)^{-B'} - 1 \right] \quad 6.1$$

Where B_0 is the bulk modulus and B' is the first derivative of the bulk modulus and V is the volume. The data were fitted with the program EosFit7 GUI [Angel,2014]. During the fitting process, the values of V_0 , B_0 and B' were left to vary freely. As the data could not be fitted in a satisfactory way with one equation of state, two different equations were chosen.

The first equation describes the behavior of the unit cell volume up to 2GPa. It is represented by the black line in (Figure 7.5). The corresponding values are $V_0=196.3085\text{\AA}^3$, the bulk modulus $B_0=110.6745$ GPa and $B'=7.555$. The second equation was used for the higher pressure range from 2 to 11 GPa and is shown as a red line in (Figure 7.5). For this EoS the fitted values are $V_0=196.45\text{\AA}^3$ with the bulk modulus $B_0=103.93\text{GPa}$ and with $B'=6.2563$.

7.3 Pressure Dependence of the Interatomic Distances in Mn₄FeSi₃

To characterize the effect of pressure on the crystal structure of Mn₄FeSi₃ the change in the atomic coordinates and interatomic distances as a function of pressure were analyzed in detail. As the unit cell parameters from the powder data are more precise than the ones obtained in a single crystal experiment, the individual values of the lattice parameters for the pressures at which the single crystal diffraction data were measured, were deduced on the basis of the two equations of state described above. The resulting values are shown in (Table 7.2). These values were used for the refinement of the single crystal data described in *chapter 5.2.4* and for the calculation of the interatomic distances.

Pressure (GPa)	0.0001 GPa	0.425 GPa	0.9 GPa	2.105 GPa	3.145 GPa	4.8 GPa	6.21 GPa
a=b (Å)	6.8834(2)	6.87458(2)	6.86521(2)	6.84195(2)	6.82242(2)	6.7936(2)	6.77093(2)
c (Å)	4.7842(2)	4.77833(2)	4.77175(2)	4.75412(2)	4.74021(2)	4.71944(2)	4.7029(2)
V (Å ³)	196.3(1)	195.6(1)	194.8(1)	192.7(1)	191.1(1)	188.6(1)	186.7(1)

Table 7.2 Lattice parameter of Mn₄FeSi₃ used for the refinement of the single crystal diffraction data. The parameters were calculated on the basis of the equations of state fitted to the powder diffraction data.

pressure GPa	x-Mn2	x-Si1
0.0001	0.76638(06)	0.59822(01)
0.425	0.76879(09)	0.59732(18)
0.9	0.76781(09)	0.5979(18)
2.105	0.76776(06)	0.59797(13)
3.145	0.76803(1)	0.59667(2)
4.8	0.7694(1)	0.598(2)
6.21	0.7701(14)	0.595(3)

Table 7.3: x-coordinates of Mn2 and Si1 on WP 6g (x,0,1/4) as a function of pressure.

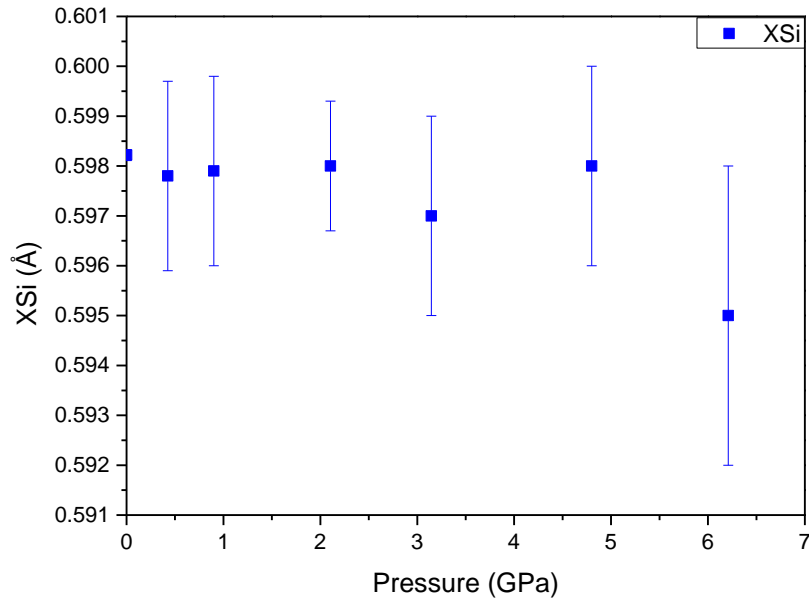


Figure 7.6: Pressure dependence of the x coordinate of the Si atom in Mn_4FeSi_3

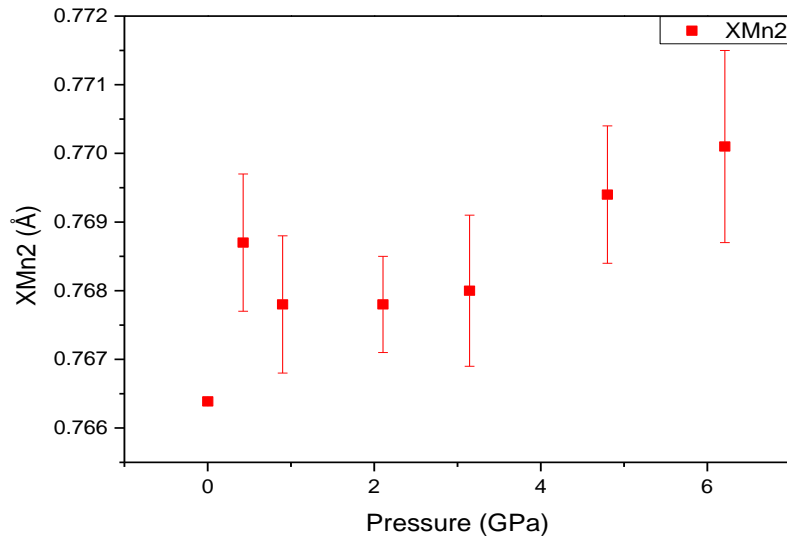


Figure 7.7: Pressure dependence of the x coordinate of the Mn2 atom in Mn_4FeSi_3

The change of the free atomic coordinates as a function of pressure is shown in (Table 7.3) and (figures 7.6 and 7.7). From the figure it is evident that the coordinates x and x' corresponding to Mn2 and Si, respectively, show a different behavior as a function of pressure. The x' coordinate of Si is within error nearly constant and only shows a slight decrease at the highest pressure reached in the experiment. However, the values of the x coordinate of Mn2 show a different behavior: they are constant at lower pressures and significantly start to increase at pressures higher than 2GPa. This pressure corresponds to the one where one needs to introduce the second equation of state (*chapter 7.1*) to describe the change of the unit cell volume as a function of pressure.

To better understand the pressure-induced effects on the crystal structure of Mn_4FeSi_3 the interatomic distances were calculated as a function of pressure (Table 7.4). (Figure 7.8) shows schematic of the structure where the individual interatomic distances are indicated. Three different trends for the interatomic distances can be observed.

- Group 1: The Fe1/Mn1 –Fe1/Mn1 distances, the Fe1/Mn1-Si1 distances, and the Si-Si distances show an almost linear decrease with increasing pressure in the whole pressure range.
- Group 2: The Mn2-Mn2' and Mn2-Mn2'' distances only decrease slightly up to 2 GPa; above 2 GPa the slope of the curve gets steeper and the decrease in the distance is more pronounced.
- Group 3: The Fe1/Mn1-Mn2 distances, and the different Mn2-Si distances decrease more in the lower pressure range up to 2GPa. Once this pressure is reached the decrease in the distances is less pronounced.

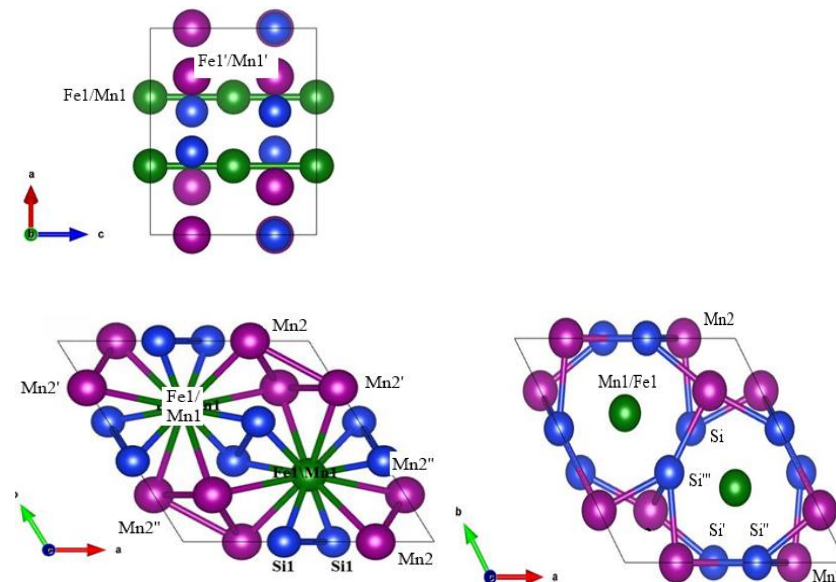


Figure 7.8: Schematic view of the crystal structure of $\text{Mn}_4\text{Fe}_4\text{Si}_3$. Mn1/Fe1 atoms are indicated in green, Mn2 atoms in magenta and Si-atoms in blue. Individual distances connecting the atoms are indicated by lines.

The first group of distances is directly related to the $[(\text{Fe1}/\text{Mn1})\text{Si}_6]$ -octahedra, which seem to be linearly compressed over the whole pressure range. The second group of distances is related to the empty $[\text{Mn2}]_6$ -octahedra. They are hardly compressed at lower pressures and start to get more compressible once the pressure of 2 GPa is reached. Finally, the distances in the third group which are related to distances between atoms of the $[(\text{Fe1}/\text{Mn1})\text{Si}_6]$ -octahedra and the $[\text{Mn2}]_6$ -octahedra show a stronger decrease in the low pressure range up to 2GPa than at higher pressures. The (Figure 7.9) shows Pressure dependence of the interatomic distances for Fe1-Mn2, Mn2-Mn2', Mn2-Mn2'', Mn2-Si1, Mn2-Si1'', Si1-Si1''' in Mn_4FeSi_3 .

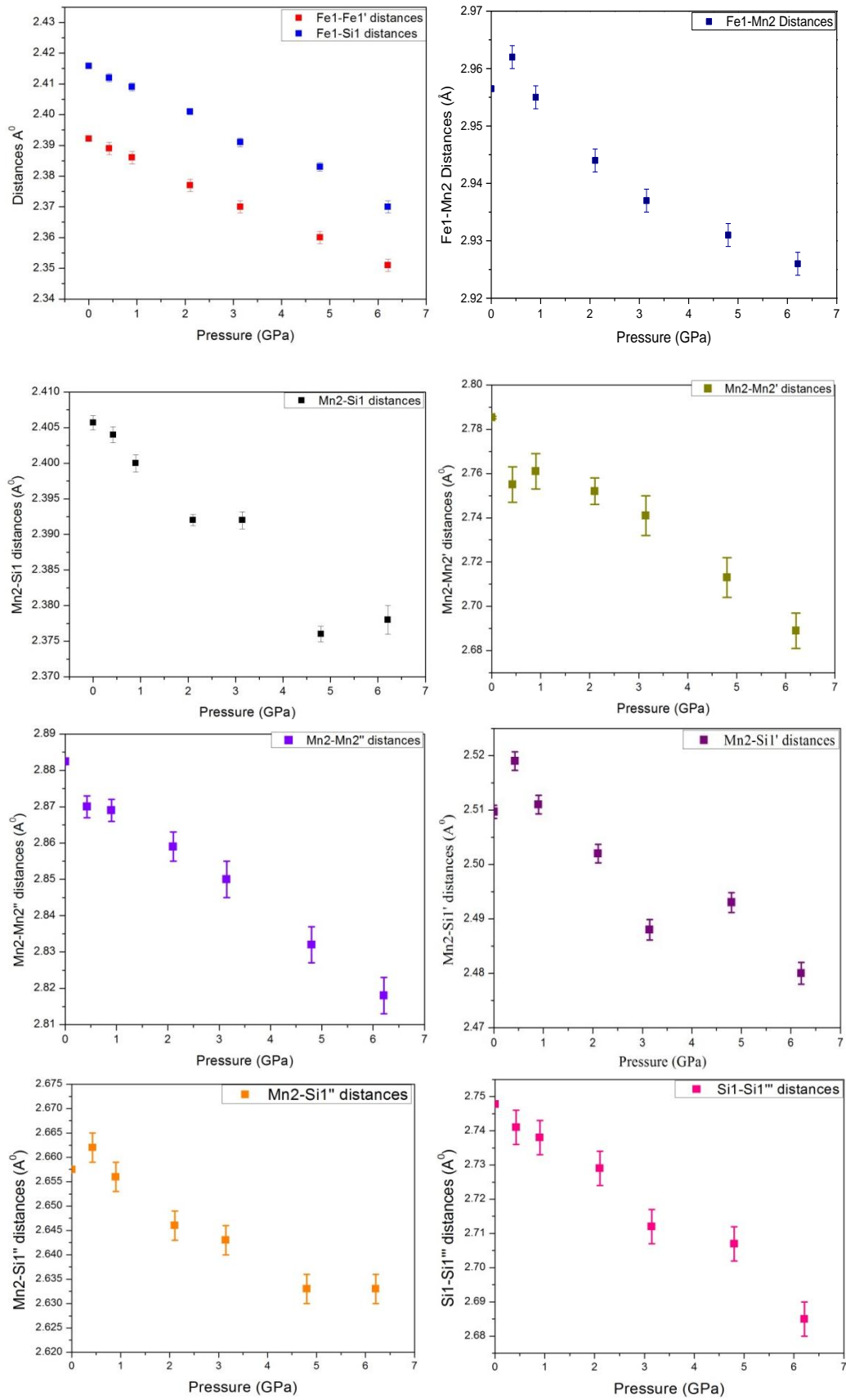


Figure 7.9: Pressure dependence of the interatomic distances for Fe1-Mn2, Mn2-Mn2', Mn2-Mn2'', Mn2-Si1, Mn2-Si1'', Si1-Si1''' in Mn_4FeSi_3 .

	0.001 GPa	0.42 GPa	0.9 GPa	2.10 GPa	3.145 GPa	4.8 GPa	6.21 GPa
Fe1-Fe1' 2x	2.3921(3)	2.389(2)	2.386(2)	2.377(2)	2.37(2)	2.36(2)	2.351(2)
Fe1-Mn2 6x	2.9565(5)	2.962(4)	2.955(4)	2.944(4)	2.937(5)	2.931(5)	2.926(7)
Fe1-Si1 6x	2.4158(9)	2.412(13)	2.409(13)	2.401(11)	2.391(14)	2.383(14)	2.37(2)
Mn2-Mn2' 2x	2.7853(6)	2.755(8)	2.761(8)	2.752(6)	2.741(9)	2.713(9)	2.689(14)
Mn2-Mn2'' 4x	2.8824(4)	2.87(3)	2.869(3)	2.859(4)	2.85(5)	2.832(5)	2.818(5)
Mn2-Si1 2x	2.4057(1)	2.404(11)	2.4(12)	2.392(8)	2.392(12)	2.376(11)	2.378(2)
Mn2-Si1' 1x	2.5097(12)	2.519(17)	2.511(11)	2.502(7)	2.488(19)	2.493(18)	2.48(3)
Mn2-Si1'' 2x	2.6575(5)	2.662(8)	2.656(5)	2.646(4)	2.643(8)	2.633(8)	2.633(13)
Si1-Si1''' 2x	2.7478(5)	2.741(7)	2.738(7)	2.729(5)	2.712(7)	2.707(7)	2.685(1)

Table 7.4: Interatomic distances in Mn₄FeSi₃ in [Å] as a function of pressure.

7.4 Effect of Pressure on the Crystal Structure of Mn₄FeSi₃

The compound Mn₄FeSi₃ (space group P6₃/mcm) is stable over the whole pressure range which was studied in this work and no indications for a change of symmetry have been found. At approximately 2 GPa an anomaly is observed in the pressure dependence of the unit cell volume and two equations of state (below and above 2GPa) have to be used. The anomaly at 2GPa is also reflected in the free atomic coordinates, in particular of the Mn2 atom. In addition, the interatomic distances also reflect this anomaly.

The compressibility mechanism can be described in the following way: at pressures up to 2GPa the distances between the two different types of octahedra [Mn1/Fe1Si₆] and [Mn2]₆ are the most compressible ones. Above 2 GPa, these distances get less compressible and instead the [Mn2]₆-octahedra show an increase in compressibility. The [Mn1/Fe1Si₆]-octahedra show a linear compressibility over the whole pressure range and do not reflect the anomaly at 2GPa. Further investigations (*see Chapter 8*) are necessary to elucidate the underlying mechanism in more detail.

Chapter 8 Summary and Conclusions

In order to determine the limits of stability of the Mn_4FeSi_3 compounds, we have performed in-situ single-crystal and powder diffraction experiments at ambient pressure and high pressure.

- On the basis of these data the crystal structure of MnFe_4Si_3 was determined at ambient pressure. The results basically confirm the model from earlier investigations, yet - in contradiction to what has been observed earlier - our calculations show that Fe is only incorporated into one of the available sites.
- In situ high pressure powder X-ray diffraction experiments using synchrotron radiation were carried out up to 10.92 GPa on Mn_4FeSi_3 . From these data the pressure dependence of the lattice parameter and unit cell volume was determined. The pressure dependence of the unit cell volume was fitted with two equations of state, one for the pressure range 0-2 GPa (with $V_0=196.3085\text{\AA}^3$ and the bulk modulus $B_0=110.6745$ GPa) and a second one for the pressure range from 2-10.92 GPa ($V_0=196.45\text{\AA}^3$ and the bulk modulus $B_0=103.93$ GPa).
- The change in the lattice parameter a (b) and c in the investigated pressure range is approximately 2.6%, the unit cell volume is decreased by approx. 7.6%. The compression is highly isotropic as the decreased of the $a(b)$ and the c lattice parameter are basically identical.
- The pressure dependence of the crystal structure was studied in the pressure range up to 6.21 GPa and full structure refinements based on single crystal data were carried out for six different pressure points. They show that Mn_4FeSi_3 crystallizes in space group $P6_3/mcm$ in the whole pressure range.
- Pressure-induced changes in the free coordinates and interatomic distances were studied in detail and further hint towards an anomaly at approx. 2GPa. The different coordination polyhedra show different behavior as a function of pressure. A general description of the compressibility mechanism was provided.

To elucidate the anomaly of the structural parameters at approx. 2GPa further investigations are warranted. In particular, magnetization measurements and neutron diffraction experiments under pressure should be performed to find out whether the structural anomaly is related to a change in magnetic ordering and could thus provide direct hints to the underlying mechanism of the magnetocaloric effect in the compounds of the system $\text{Mn}_{5-x}\text{Fe}_x\text{Si}_3$.

Bibliography

[Binczyska et al, 1973]. H. Binczyska, Z. Dimitrijevic, B. Gajic, et. al., *Phys. Stat. Solidi* A19, 13, (1973).

[Johnson, 1972]. V. Johnson, D. B. Rogers, J. F. Weiher, et. al., *J. Solid State Chem.* 4311, (1972).

[Songlin et al, 2002]. Songlin, Dagula, O. Tegus, et. al. *J. Alloys Comp.* 334, 249, (2002).

[Landau, 2007]. David P. Landau, *Theory of Magnetic Phase Transitions*, Handbook of Magnetism and Advanced Magnetic Materials, (2007).

[Oliveira et al, 2002]. N. A. de Oliveira and P.J. Ranke, *Phys. Rep.* 489, 89, (2010).

[Tegus et al, 2002]. O. Tegus, E. Brück, K. H. J. Buschow, and F. R. de Boer, *Nature* 415, 450, (2002).

[Candini et al, 2004]. A. Candini, O. Moze, W. Kockelmann, et. al., *J. Appl. Phys.* 95, 6819, (2004).

[Röntgen, 1895]. Röntgen, W. C. Übereineue Art von Strahlen. *Sitzungsber. Der Würzburger Physik-Medic. Gesellsch.* 137, 132–141 (1895).

[Laue, 1912]. von Laue. "Concerning the detection of x-ray interferences". Nobel Lectures, Physics. (1901–1921). Retrieved (2009).

[Friedrich, 1912] Friedrich, W. , Knipping, P. & Laue, M. *Interferenz-Erscheinungen*, 303–322 (1912).

[Wikipedia, 2015]. *Bragg's law*. [Online; accessed 29-January -2015].
http://en.wikipedia.org/wiki/Bragg%27s_law.

[Ewald, 1913]. *Ewald PP*, *Physik. Z.*, 14, 465-472, (1913).

[Massa, 2004] Werner Massa. *Crystal Structure Determination, second edition* ,pp 30, (2004).

[Klaus-Dieter et al, 2003]. Liss, Klaus-Dieter; Bartels, Arno; Schreyer, Andreas; Clemens, Helmut "High-Energy X-Rays: A tool for Advanced Bulk Investigations in Materials Science and Physics." 35 (3–4): 219, (2003).

[Binczyska et al, 1973]. H. Binczyska, Z. Dimitrijevic, B. Gajic, et. al., *Phys. Stat. Solidi* A19, 13, (1973).

[Jouan, 1996]. S. Merlin, A. Jouan, JP. Moncouyoux and P. Roux. *Multiple Applications of Cold Crucible Melting. Waste Management' 96*, Tucson, (1996).

[Beys and Gier, 2014] M. Beys and H. Gier. Poster, Schmelzverfahren für die Herstellung von Reinstmaterialien. Forschungszentrum Jülich GmbH, Forschungszentrum Jülich GmbH, (2014).

- [**Czochralski, 1918**]. J. Czochralski, *A new method for the measurement of the crystallization rate of metals*, *Zeitschrift für Physikalische Chemie*, **92** : 219–221, (1918).
- [**Gottschlich, 2013**] Michael Gottschlich, *Structure magnetism and excitations in some Mn-based magnetocaloric effect compounds*, PhD Thesis, Forschungszentrum Jülich, p 20, 2013.
- [**xray.chem, 2010**]. *Introduction to Crystallography*. [Online; accessed 20-12 -2014]. <http://xray.chem.wisc.edu/Welcome.html>.
- [**Ladd and Palmer, 2003**]. Mark Ladd, Rex Palmer. *Structure Determination by X-ray Crystallography*, 4th Edition, Springer (2003).
- [**Forman et al, 1972**]. R. A. Forman, G. J. Piermarini, J. D. Barnett, and S. Block, *Pressure Measurement Made by the Utilization of Ruby Sharp-Line Luminescence*, *Science* 176, 284-285, (1972).
- [**Mao and Bell, 1979**]. Mao, H. K. and Bell, P. M., *Observations of Hydrogen at Room Temperature and High Pressure*, *Science* 203 1004, (1979).
- [**Yang and Dong, 2011**]. Song Yang¹ and Dong Zhaohui, *Novel Pressure - Induced Structural Transformations of Inorganic Nanowires*, pp. 527-551, (2011).
- [**Katrusiak, 2008**]. Andrzej Katrusiak, *High-pressure crystallography*, *Acta Cryst. A* 64, 135–148, (2008).
- [**Boehler, 2006**] R. Boehler, *Rev. Sci. Instr.* 77, 115103, (2006).
- [**Valkenburg, 1962**]. Alvin Van Valkenburg, *Visual Observations of High Pressure Transitions*, *Rev. Sci. Instrum.* 33, 1462, (1962).
- [**Piermarini and Barnett, 1976**]. Block, S. and Piermarini. *The diamond cell stimulates high-pressure research*, *Physics Today* 29(9), pp. 44–7, (1976).
- [**Seda, 2005**]. Takele Seda, *High pressure methodology*, Western Washington University Department of Physics and Astronomy. (2005).
- [**Perlan, 2010**] *Agilent technologies*. [Online; accessed 2-February -2015]. <http://www.perlan.com.pl/media/xrd/SuperNova.pdf>.
- [**Busing, 1967**]. Busing WR, Levy HA, *Angle calculations for 3- and 4- circle X-ray and neutron diffractometers*. *Acta Crystallography* 22:457-464, (1967).
- [**Coppens, 1970**] P. Coppens in *Crystallographic Computing* F.R. Ahmed, S.R. Hall and C.P. Huber, Copenhagen, Munksgaard, pp 255-270, (1970).
- [**jana2006, 2010**]. *Jana2006* [Online; accessed 13-February -2015]. <http://jana.fzu.cz/>
- [**Jana2006, 2006**] *Jana2006- Computer program*, V. Petricek, M. Dusek, L. Palatinus, Institute of Physics, Academy of Sciences of the Czech Republic, Praha, (2006).
- [**Jones, 1979**]. P. G. Jones, *Crystal Structure Determination: A Critical View*, New York, (1979).

- [**Hering et al, 2014**] Paul Hering, Th. Brückel, habil. K. Friese, J. Voigt *Studium des Magnetokalorischen Effekts in $MnFe_4Si_3$* , Aachen, 31.01.(2014).
- [**X-Area, 2006**]. *Stoe X-Area Software Manual*, STOE&Cie GmbH, 2006.
- [**Angel, 2013**]. RJ Angel, ABSORB 7 Manual, *Ross Angel Software*, January(2013).
- [**Friese, 2013**]. Friese K, Grzechnik A, Posse JM, Petricek V., Refinement of high pressure single-crystal diffraction data using Jana 2006, *High Press. Res.* 196–201,(2013).
- [**Bauchau et al, 1998**] Thoms M, Bauchau S, Häusermann D, Kunz M, LeBihan T, Mezouar M, Strawbridge D, An *improved X-ray detector for use at synchrotrons*. Nucl Inst Meths Phys Res A413:175-184, (1998).
- [**Letoullec 1998**] R. Letoullec, J.P. Pinceaux, P. Loubeyre: *The membrane diamond anvil cell: a new device for generating continuous pressure and temperature variations*, *High Pressure Research I*, 77-90, (1988).
- [**Hammersley, 1996**] A. P. Hammersley, S. O. Svensson, M. Hanfland, A. N. Fitch, and D. Häusermann, ``*Two-Dimensional Detector Software: From Real Detector to Idealised Image or Two-Theta Scan*`, *High Pressure Research*, **14**, pp235-248, (1996).
- [**Lebail, 1988**] A. Lebail, H. Duroy, J. L. Fourquet: *Ab initio structure determination of $LiSbWO_6$ by X-ray powder diffraction*, Mat. Res. Bull. 23, 447-452 (1988).
- [**Murnaghan, 1944**]. F.D. Murnaghan, Proc. of the Nat. *Academy of Sciences* (USA) **30**, 244 ,(1944).
- [**Thibault, 2009**]. P. Thibault, *A Review of Equation of State Models, Chemical Equilibrium Calculations and CERV Code Requirements for SHS Detonation Modelling*, (2009).
- [**Angel, 2014**] *EosFit*. [Online; accessed 20-june -2015]. http://www.rossangel.com/text_eosfit.htm
- [**esrf, 2015**]. ID09A - White Beam Beamline, High Pressure Station. [Online; accessed 1-june - 2015]. <http://www.esrf.eu/UsersAndScience/Experiments/DynExtrCond/ID09A>.
- [**Stoe Face, 2007**]. Stoe Face It Video, *Operation Manual*, STOE& CIE GmbH, November, 29th (2007).

التركيب البلوري للمركب الحراري (Mn_4FeSi_3) تحت الضغط العالي

اعداد الطالب: محمد اكرم نمر مسودة

اشراف:

البرفسور: سلمان سلمان - فلسطين

البرفسور: كارين فريزي - ألمانيا

الملخص

المركب المغناطيسي الحراري المستخدم في هذه التجربة هو Mn_4FeSi_3 هو بلورة سداسية الشكل وينتمي إلى مجموعة التماثل ($P6_3/mcm$) في الظروف المحيطة ، إن محور العمل يتركز على تحليل التركيب البلوري لمركب Mn_4FeSi_3 تحت الضغط العالي عن طريق استخدام حيود الأشعة السينية المنعكسة عن مسحوق المركب أو عن بلورة واحدة ، حيث يتم القياس في المختبرات باستخدام أجهزة تصدر الأشعة السينية أو مصدر السنكروترون، حيث يتم تحمل العينة داخل جهاز الضغط المسمي خلية سندان الماس "Diamond anvil cell"، إن إجراء القياسات يتم في نطاق ضغط يتراوح بين 0.0001 جيجا باسكال إلى 6.21 جيجا باسكال.

التغيرات التي قد حصلت في التركيب البلوري من اختلف المسافة بين الذرات وانكماش حجم وحدة الخلية عند تطبيق الضغط الهيدروستاتيكي يتم وصفه بالتفصيل في هذه الدراسة.